U.S. National Library of Medicine
National Center for Biotechnology Information

NLM Citation: Tax CMW. Estimating chemical and microstructural heterogeneity by correlating relaxation and diffusion. In: Topgaard D, editor. Advanced Diffusion Encoding Methods in MRI [Internet] [Select Chapters]. Cambridge (UK): Royal Society of Chemistry; 2020 Aug. Chapter 7. doi: 10.1039/9781788019910-00186
Bookshelf URL: https://www.ncbi.nlm.nih.gov/books/

7. Estimating chemical and microstructural heterogeneity by correlating relaxation and diffusion

Chantal M.W. Tax[a]

Abstract

Whereas diffusion NMR can probe the structural configurations of microscopic environments in biological tissue, relaxation can provide complementary information on their chemical composition. This chapter considers experiments in which diffusion and relaxation properties are sampled simultaneously by varying multiple acquisition parameters. As such, correlations between the diffusion and relaxation can be established, providing an altogether more complete picture of heterogeneous tissue.

7.1. Introduction

The previous chapters have dealt with the use of magnetic resonance to track the translational motion of molecules. *Multi-dimensional diffusion MR* encodes the signal in multiple dimensions; e.g., two successive pulsed-gradient pairs in different directions. If molecules experience hindered diffusion in locally anisotropic micro-domains, the signal attenuation will depend on the relative orientation of the pulses. As shown in Chapter 3, this can thus be used to characterise local anisotropy even if the orientation distribution of the domains is globally random.

The experiment with two successive pulsed-gradient pairs in different directions is part of a much broader class of experiments based on the concept of multiplexing[1] in which multiple signals are combined into one signal. In the context of MR, this means that the signal is encoded as a function of multiple experimental parameters. In contrast to separately acquiring each dimension, multi-dimensional MR can be used to estimate the *joint distribution* and as such establish *correlations* between the dimensions.

Author Affiliation: a Cardiff University Brain Research Imaging Centre (CUBRIC), Cardiff University, Maindy Rd, Cardiff CF24 4HQ, United Kingdom; Email: taxc@cardiff.ac.uk.

Corresponding author.

This is the manuscript of a chapter accepted for publication by the Royal Society of Chemistry in the book *Advanced Diffusion Encoding Methods in MRI* published August 2020.

Peemoeller et al. (1981)[2] describes one of the earliest multi-dimensional MR experiments of relaxation times in wet hen egg-white lysozyme. They analysed the data using a graphical method called *curve peeling*, which does not require non-linear curve fitting to extract exponentials. In multi-dimensional experiments, a multiexponential decomposition can then be graphically performed in each dimension. English et al. (1991)[3] later introduced numerical methods, which were not biased by a priori assumptions on the number of components and yielded reproducible results. Since then, many approaches have been proposed to numerically estimate correlation spectra[4–7].

This chapter focuses on the *correlation of diffusion and relaxation*, for which the mathematical formulation was already presented in the 70s[8]. Heink et al. (1991)[9] observed an interaction between diffusion and relaxation: the estimated apparent diffusivity turned out to depend on the echo time (TE), and this was initially treated as an artifact. Van Dusschoten et al. (1995)[10] later exploited this as a contrast to sensitise the signal to the different physical phenomena underlying diffusion and relaxation. Since then, diffusion-relaxation correlation has been applied to a wide range of porous media, e.g. in sedimentary rocks[11–14], cheeses and other dairy products[15,16], liquid crystals[5,17], glass beads[18,19], drugs[20], crude oils[21,22], hydrogels[23], plants[10,24,25], and yeast cells[26]. It has even been implemented to be used with inhomogeneous low magnetic fields without pulsed gradients: a permanent magnet with a static gradient and a basic NMR spectrometer greatly facilitates application in large substances[16].

Multi-dimensional diffusion-relaxation correlation experiments are becoming more popular in human MRI[27–38]. In current clinical practise, routinely acquired MR-images still largely show *qualitative* tissue-contrast, with intensities arbitrarily scaled according to different MR-phenomena. In contrast, *quantitative* MRI aims to extract reproducible measures more directly related to tissue properties. Diffusion-relaxation correlation increases the quantitative potential of MRI and as such can have important clinical ramifications in disease management and diagnosis. This chapter will focus on diffusion-relaxation correlation in animal and human tissue, in the light of its potential implications on clinical MRI.

The chapter is structured as follows. Section 7.2 will briefly answer the question "what is relaxation?", complementing the extensive discussions in the previous Chapters on the process of diffusion. Section 7.3 will give an overview of studies that have performed diffusion-relaxation correlation in animal tissues, answering the question "why complement diffusion with relaxation?". This Section is structured according to four commonly reported key benefits of diffusion-relaxation correlation over either diffusion- or relaxation-MR alone: 1) it provides additional voxel-wise information, 2) multiple components per voxel can be better disentangled, 3) it can stabilise the fitting in either the diffusion or relaxation dimension, and 4) it can ameliorate the issue of diffusion MR providing T_2-weighted signal fractions in the case of multiple components. Section 7.4 briefly discusses "how to measure diffusion and relaxation simultaneously?", where the reader is also referred to Chapter 9 for a more detailed description on acquisition. Section 7.5 considers the topic "how to estimate diffusion and relaxation?", introducing free inversion and model-based estimation (Chapters 11 and 12). Finally, Section 7.6 will review the question "how to validate diffusion-relaxation correlation?", and Section 7.7 discusses limitations and future outlooks.

7.2. What is relaxation?

Relaxation is the process of spins returning to their thermal equilibrium state with time, after they have been brought into an excited state. T1 and T2 relaxation describe two different processes affecting the nuclear magnetisation; both have a complex relation to material properties. Relaxometry has been extensively used to quantitatively characterise a wide range of materials (see e.g.[39] for an overview in liquids and[40] in brain). In biological tissues, relaxation can originate from phenomena on different scales: the molecular nanometer scale, the cellular micrometer scale, and the MRI resolution millimetre scale[41–43]. Here, we give a brief overview of the different relaxation processes.

7.2.1. Longitudinal relaxation

Longitudinal relaxation, or spin-lattice/thermal/T1 relaxation, is the recovery of the longitudinal (i.e. in z-direction) nuclear spin magnetisation towards the thermal equilibrium. The T1 value is the time it costs for the longitudinal magnetisation to recover to 63% (i.e. $1 - \exp(-1)$) of its initial value after a 90° RF pulse. On the molecular scale, longitudinal relaxation involves a redistribution of spin-up and spin-down populations for which the energy gained from the RF pulse must leave the spin system. To this end, the spins have to exchange energy with their surroundings (the lattice) as spontaneous emission is unlikely in the frequency range of NMR. The most efficient longitudinal relaxation occurs when protons or electrons on the same or neighbouring molecules cause locally fluctuating magnetic fields near the Larmor frequency[44]. The optimal 'interaction distance' in MRI is in the order of nanometers, and the values of T1 are mainly given by cross-relaxation between water and the macromolecules in tissue[45].

7.2.2. Transverse relaxation

Transverse relaxation, or spin-spin relaxation, is the decay of the net transverse magnetisation (i.e. in the xy-plane) due to dephasing of the individual spins. The T2 value is the time it costs for the transverse relaxation to decay to 37% (i.e. $\exp(-1)$) of its initial value after a 90° RF pulse. The T2 effect, in contrast to T1, can originate from different scales and is mostly caused by a variation in the magnetic field. On the molecular scale, the magnetic field changes due to random rotation of the molecules (and the associated dipole fields of their protons). In the presence of large molecules, this motion slows down and the relaxation rate ($R_2 = 1/T_2$) increases[44]. In addition, if a spin that contributes to the net transverse magnetisation exchanges energy with the lattice following T1 relaxation, then it will also lose phase coherence with other spins.

Magnetic susceptibility is an inherent property of a material and describes the relation between an externally applied magnetic field and the field within the object. In composite materials the magnetic susceptibility varies with position in space, which leads to spatial variation of the local magnetic field. On the cellular scale (also referred to as microstructural or mesoscopic scale), the presence of paramagnetic substances induces an additional magnetic field that varies in space and time. This causes additional dephasing of spins not only in the immediate neighbourhood of the substance, but also on larger length scales depending on the size and geometry of the compartment in which the substance is residing. In porous media such as sedimentary rocks, paramagnetic ions on or near the surface cause enhanced relaxation of fluid molecules near the surface, also called surface relaxation[46]. This has been used to study the surface-to-volume ratios of pores[47]. In biological tissue, iron associated with hemoglobin in blood or in cells (e.g. in deep gray matter nuclei in the brain) cause additional transverse relaxation.

Even if the field inhomogeneities are static (that is, they don't change over time), the spins probe different magnetic susceptibilities over time if they exhibit non-negligible diffusion. As such, the measurement becomes sensitive to the spatial correlations of the susceptibility. Part of this relaxation cannot be fully refocused, as the effect of diffusion cannot be undone. The behaviour of the transverse relaxation as a result of diffusion in inhomogeneous fields has been investigated in several works[18,48–50].

Finally, on the macroscopic scale of the MRI voxel size, inhomogeneities can be caused by differences in macroscopic susceptibility between tissues, e.g. at the air-tissue interface near sinuses in the brain, by poor shimming, and by the sample shape. The effect of diffusion can be neglected at this scale, and dephasing due to these inhomogeneities can in principle be fully rephased by the spin-echo experiment. The classic equation for NMR in chemical solutions separates relaxation from macroscopic origins (denoted by R_2'):

$$R_2^* = R_2 + R_2', \quad [2]$$

7.3. Why complement diffusion with relaxation?

7.3.1. Additional information

From the previous section, it is obvious that relaxation provides a rich source of information that is complementary to diffusion; whereas diffusion NMR provides information on molecular motion, relaxation provides information on the molecular interactions of the system of spins, amongst others. Hutter et al. (2018)[28] showed scatter plots of estimated voxel-wise T1, T2*, and diffusivity in the living human brain, revealing the independence of these tissue parameters and thus the benefits of acquiring multiple dimensions (Figure 7.1a). Simultaneous quantification of voxel-wise NMR properties (the NMR 'fingerprint'[51]) can improve the classification of tissues, and as such the diagnostic capability in medical applications. This was for example demonstrated by Yu et al. (2017)[52], who performed T1, T2, and diffusivity mapping in prostate and showed that tissue manually classified as prostate cancer had lower estimated T1, T2, and D than normal tissue. Combined contrasts (specifically the estimation of voxel-wise D and T2, Figure 7.1b) had a better separation between different tumour grades than single contrasts.

Figure 7.1. Diffusion-relaxation correlation gives additional information. Here, one D and one T2 and/or T1 per voxel were estimated and then distributions across voxels are shown.

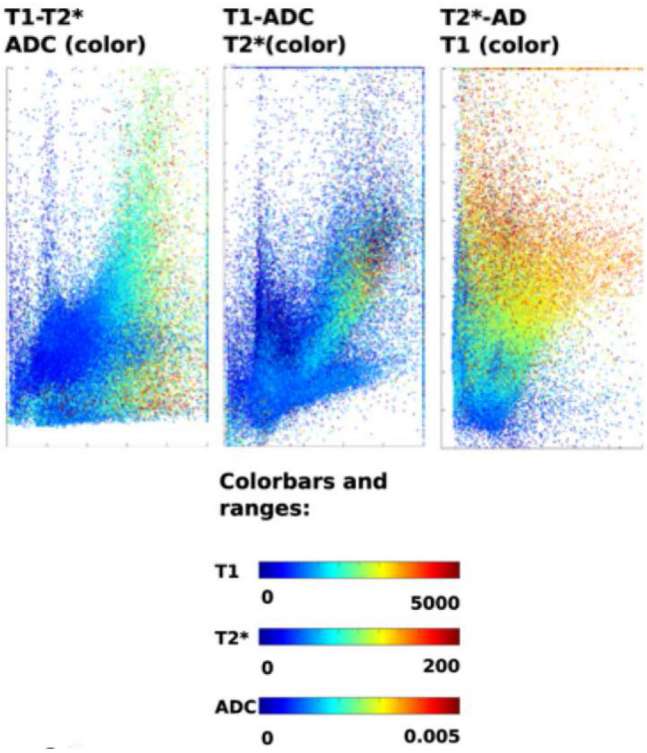

a). In healthy controls, scatter plots between voxel-wise T2, T1, and D reveal independence between parameters.

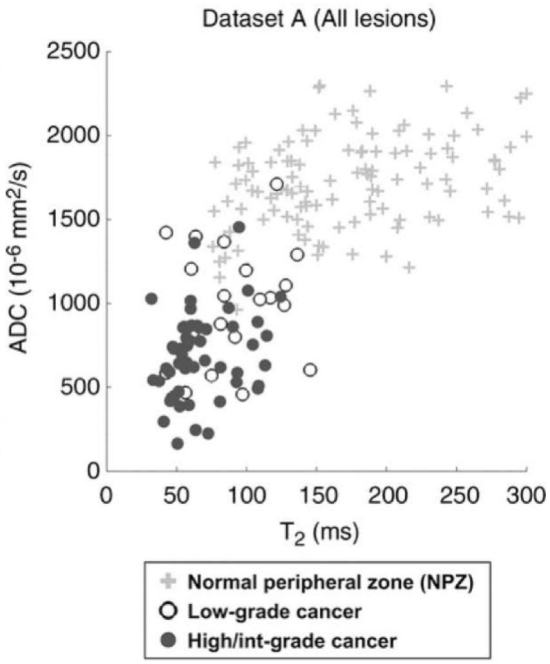

b). In prostate cancer patients, D and T2 were significant predictors for differentiating between histologically proved high- or intermediate-grade tumours and low-grade tumours.

Adapted from[52] with permission from RSNA, Copyright 2017.

7.3.2. Resolving multiple components

For simple systems such as water in aqueous solutions, all the molecules sense the same environment and the material can thus be described with a single T1, T2, and D (also the assumption in most MR fingerprinting approaches). For complex systems such as porous rock, food, and biological tissue, the molecules can reside in different microscopic environments (e.g. inside and outside cells in tissue). As such, different molecules can sense different microscopic environments, and the material is better described by distributions of T1, T2, and D within a voxel (as opposed to Figure 7.1 where distributions of voxel-wise T1, T2, and D across voxels are shown).

The 1D distributions of NMR observables in heterogeneous materials are often quite broad, and hence 1D experiments might struggle to resolve separate components in these materials. Multi-dimensional experiments, in contrast, can rely on measurements of different underlying physical processes (e.g. relaxation and self-diffusion) to disentangle compartments and thus have the potential to improve the resolving power of NMR. Instead of just acquiring different 1D experiments, multi-dimensional correlation experiments – in which the signal attenuation is acquired by varying multiple experimental parameters simultaneously – are required to resolve the *joint distribution* of the different NMR observables. Indeed, this principle was first demonstrated in a 2D T1-T2 experiment in excised rat muscle[3], where independent 1D experiments failed to resolve all components.

Diffusion-relaxation correlation, which is the focus of the current Chapter, has shown to be a powerful tool to disentangle components that are different in size/shape and chemical composition. The next subsections will focus on experiments to investigate compartmentalisation in animal and human tissue.

7.3.2.1. In vitro NMR

Nervous tissue – which is commonly compartmentalised into water residing between the myelin sheets, within the axons, and outside the axons (Figure 7.2a) – has been studied extensively with diffusion-relaxation correlation. Beaulieu et al. (1998)[53] sought to provide evidence of compartmentalisation in nerve water T2 and D by using three different excised nerves of the garfish; non-myelinated olfactory nerve, trigeminal nerve myelinated by Schwann cells, and optic nerve myelinated by oligodendrocytes. They indeed found three T2 components in myelinated nerves but only two in the non-myelinated nerves. They did not find any dependence of the measured apparent diffusivity and anisotropy on the T2 component of origin. Stanisz and Henkelman (1998)[54], in contrast, found that diffusion was more anisotropic in the longest T2-component than in the shortest T2-component in the bovine optic nerve, where the latter is often associated with water confined within myelin. Peled et al. (1999)[55] found three T2 compartments in the frog peripheral nerve, where the shortest T2 compartment showed some restriction, the intermediate T2 compartment showed relatively high and unrestricted diffusion, and the longest T2 compartment showed restricted diffusion. The latter two compartments were assigned to extracellular and intracellular (most likely axonal) water. Andrews et al. (2006)[56] studied the diffusion-T2 characteristics of myelin water specifically, where they also used T1 characteristics to nullify non-myelin water. They found a lower perpendicular diffusivity, and thus higher degree of anisotropy, than Stanisz and Henkelman (1998)[54].

Other excised tissues and cells have been studied with diffusion-relaxation correlation NMR. Pfeuffer et al. (1998)[57] used diffusion-T2 relaxometry to investigate the intra and extracellular water signal and water permeability in Xenopus Laevis oocytes and glial cells. Li et al. (1998)[58] report that integrated D-T2 experiments result in better parameter determinations in a three-pool model of water in human blood. Seland et al. (2005)[59] show two components in rat myocardium with distinctly different diffusivity and T1, which they assign to intra- and extra-cellular water. Mailhiot et al. (2018)[60] show two components in porcine articular cartilage with a common D value but different T2 values.

7.3.2.2. Animal MRI

When combined with imaging, one can spatially map different components to study variations across the tissue[19]. Several studies have performed diffusion-relaxation correlation MRI in animals, both *ex vivo* and *in vivo*.

Ex vivo diffusion-relaxation correlation MRI experiments have been reported in mouse and rat spinal cord, and rat brain, amongst others. Kim et al. (2017)[61] measured diffusion and T2 relaxation in ex vivo mouse spinal cords, which revealed two different peaks to disentangle white matter, which contains the axons, and gray matter, which contains mostly cell bodies. They found an additional peak in injured cords that could not be found in healthy controls. Compared to the 2D approach, there was considerable ambiguity in the 1D diffusion and 1D relaxation spectra which made it difficult to interpret them in a meaningful way. Benjamini and Basser (2017)[62] performed D-T2 experiments in dissected rat spinal cord, and found evidence for three distinct components within the gray matter, which they assign to intracellular/neuronal soma (lower D), interstitial (higher D), and myelin-associated (lower T2) spaces. They show that the intracellular T2 is slightly longer than the extracellular T2. In white matter, two components were found that were assigned to interstitial and myelin-associated spaces, and an additional two components that were assigned to intracellular spaces: one longer T2-component that was also found in gray matter and assigned to glial soma water, and one shorter T2-component assigned to intra-axonal water. De Santis et al. (2016)[63] correlated diffusion tensors and T1-values in two excised porcine nerve fibres with very different myelination that are crossing each other at an angle. Both fibres exhibit very different T1 values in the crossing area when combined diffusion-relaxation information is into account, whereas 1D T1-relaxometry fails to recover two distinct T1s. This was also seen in perfused rat brain, where the estimated T1s were different in two crossing fibres (cingulum and genu of the corpus callosum).

In vivo diffusion-relaxation correlation MRI experiments have been reported in rat brain, rat trigeminal nerve, and cat brain, amongst others. De Santis et al. (2016)[63] extended their D-T1 MRI experiment to in vivo rat brains, and showed that the cingulum consistently exhibited higher T1 than the corpus callosum and that the more restricted population had a higher T1 in the cortex and the gray matter, but a smaller T1 in the white matter. van Dusschoten et al. (1996)[64] performed diffusion-T2 correlation in healthy cats and cats with ischemic regions following a middle cerebral artery occlusion. They found that the properties of cerebral spinal tissue and brain tissue could be more reliably analysed than with separate measurements. In addition, whereas they did find a lower diffusivity for the compartment associated to the ischemic region, they did not find T2 changes in the compartment associated to 'normal' brain tissue in ischemic regions. Does and Gore (2000)[65] imaged healthy and ischemic rat trigeminal nerve and brain, and found no proof of compartmentalisation in brain, possibly due to relatively rapid exchange between intra- and extra-cellular compartments. Two compartments were found in trigeminal nerve: water with longer T2 was found to be more restricted in perpendicular direction than water with shorter T2, possibly corresponding to extracellular and intracellular water. Myelin water was off-limits with the acquisition protocol used. Qin et al. (2009)[66] show that simulations with a longer T2 for the extracellular compartment support the observed behaviour of TE dependence in rhesus monkey. In contrast, results of De Santis et al. (2016)[67] in rat brain support a longer T2 for intra-axonal water.

7.3.2.3. Human MRI

Diffusion-relaxation correlation has also been performed in the living human brain and other organs. One major complication of in vivo human imaging is the long scan time; it takes significantly more time to adequately sample a 2D or 3D acquisition space compared to 1D (see also Section 7.4.3). Mulkern et al. (2000)[68] performed T1-D experiments to make separate measurements of T1 relaxation of the components with slow- and fast diffusion in the human brain (often associated to intra- and extra-cellular components). They did not find a significant difference, which led them to conclude that either the T1's within the compartments are similar, or the rate of water exchange is fast enough to mix the T1-relaxation behaviour of the compartments but slow enough to show a diffusion-behaviour consistent with multiple compartments. De Santis et al. (2016)[32] applied their diffusion-tensor T1 experiment to human brain, reproducing the result of different T1 values in crossing tracts. Moreover, they found a lower inter-subject variability for parameters estimated with T1-D correlation compared to T1-relaxometry alone.

Using D-T2 correlation, de Almeida Martins et al. (2019)[69] resolve five-dimensional diffusion-relaxation distributions in the living human brain (a distribution of T2s and axially symmetric tensors per voxel, the latter including perpendicular and parallel diffusivities, and two angles defining the first eigenvector). This high dimensionality allows them to resolve multiple microscopic environments within each voxel, e.g. in voxels with partial volumeing of CSF, gray matter, and white matter (Figure 7.2c). Regarding the separation of intra- and extra-axonal T2 using D-T2 correlation, Lin et al. (2018)[70] report that simulations of two hypotheses support their observations in the living human brain equally well: either the intra-axonal T2 is larger than the extra-axonal T2, or both spaces have intrinsically similar T2 but exchange with the myelin compartment causes a measurable difference. They hypothesise that the axonal membrane reduces the exchange rate between myelin water and intra-axonal water, whereas the larger interface with the extra-axonal increases the exchange with the extra-axonal water, causing the extra-axonal T2 to be reduced to a larger degree. Peled et al. (1999)[55] attribute the lower extracellular T2 to simple chemical composition effects; a higher collagen concentration in the extracellular space drives water relaxation via chemical exchange. Several studies[27,31,35], which correlate T2-relaxation and diffusion tensors, support the hypothesis of a larger intra-axonal T2 (Figure 7.2d). Various works[31,71,72] furthermore report a dependence of the voxel-wise- or intra-axonal T2 on the angle of the underlying tract relative to the main magnetic field. Ning et al. (2019)[73] show that in crossing fibre areas, different bundles were estimated to have different relaxation rates, which may have important implications for diffusion tractography. Lemberskiy et al. (2018)[74] perform D-T2 experiments in prostate and use the difference

in T2 of the cellular and luminal compartments to disentangle their contributions to the time-dependent diffusion coefficient.

D-T2* experiments have also been performed in humans. Slator et al. (2019)[75] studied the human placenta and found three components with clearly different diffusivities but similar T2*. These compartmental properties changed in patients with placentally-mediated pregnancy complications. Kleban et al. (2019)[76] aim to disentangle intra- and extra-axonal T2* using diffusion weighting, and find a significantly longer T2* for the intra-axonal compartment when the underlying fibre is perpendicular to the main magnetic field. In addition, they characterise compartmental variations in magnetic susceptibility by estimating the susceptibility-induced frequency offset, which can be interpreted as a proxy for the anisotropic susceptibility of the myelin sheath. In 1D T2*-relaxometry, including the frequency offset has shown to improve the estimation of the myelin water fraction[77], but it has also been argued that this comes at the cost of increased complexity of the fitting procedure and may therefore be ignored at field strengths of 3T and lower[78]. Joint diffusion-T2* relaxometry can provide new avenues to characterise the complementary microscopic information in the estimated frequency offset more reliably[76].

Figure 7.2. Diffusion-relaxometry can better disentangle different compartments. An example in human brain white matter and cerebrospinal fluid (CSF).

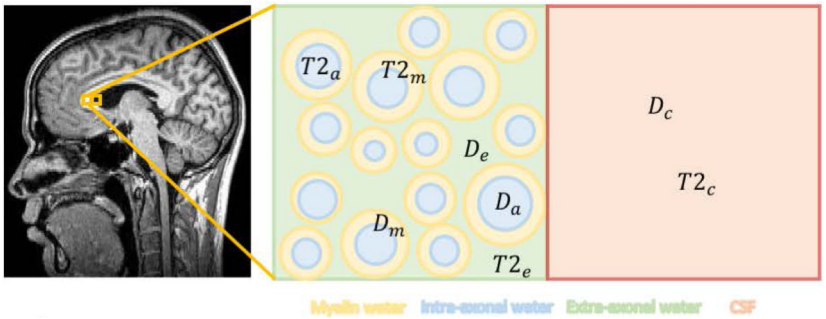

a). Schematic compartmentalisation of nervous tissue into myelin water, extra-axonal water, and intra-axonal water. Myelin is a stack of lipid bilayers and forms a concentric wrapping around the axon to 'insulate' the axon for the transmission of electrical signals; water is contained in the regions of the hydrophilic headgroups.

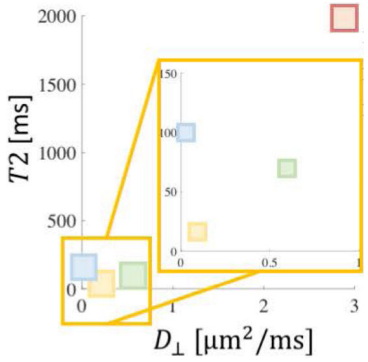

b). Schematic D-T2 spectrum for white matter.

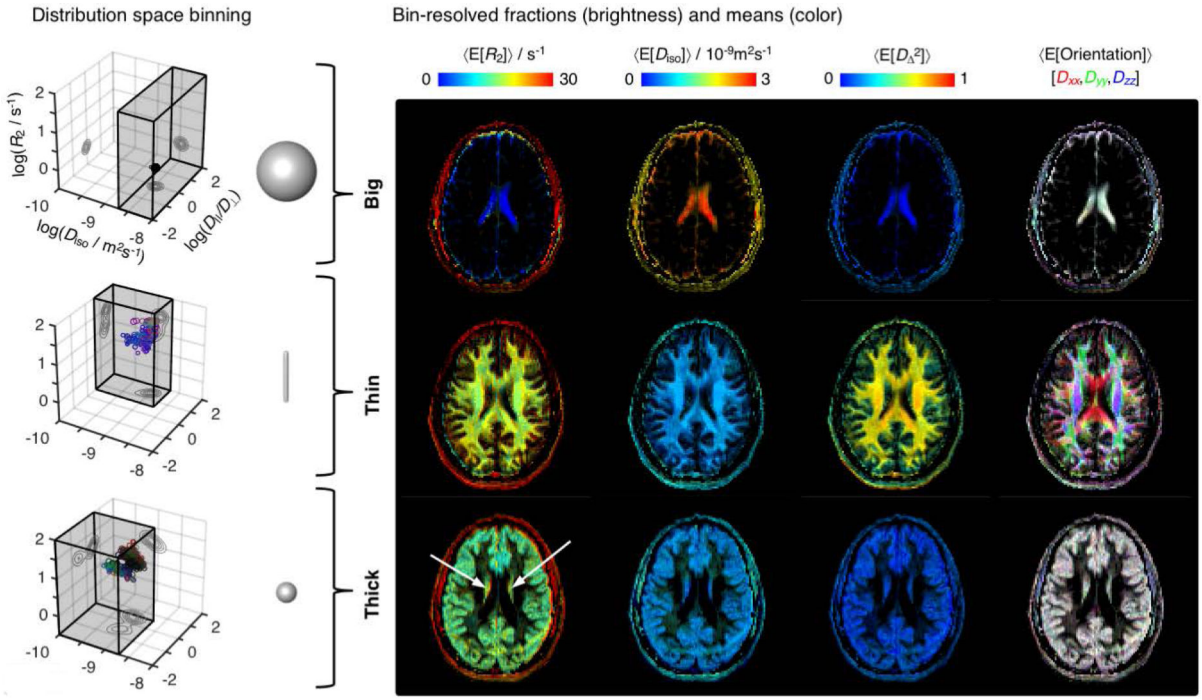

c). Left: diffusion-relaxation distributions shown as scatter plots in a 3D space of logarithms of the transverse relaxation rate R2, isotropic diffusivity D_{iso}, and axial-radial diffusivity ratio $D_{||}/D_{\perp}$ The diffusion tensor orientation (q,f) is color-coded as [R,G,B] = [cos ϕ sin θ, sin ϕ cos θ, cos θ]$|D_{||} - D_{\perp}/\max(D_{||},D_{\perp})$ and the circle size is proportional to the weight of the component. The distributions are subsequently divided into 'bins' named 'Big', 'Thin', and 'Thick' that loosely capture the diffusion features of cerebrospinal fluid CSF, white matter WM, and gray matter GM, respectively. Right: Parameter maps of average per-bin means (color) of transverse relaxation rate, isotropic diffusivity, squared anisotropy and diffusion tensor orientation, color-coded as [R,G,B] = [Dxx, Dyy, Dzz]/max(Dxx, Dyy, Dzz), where Dii are the diagonal elements of laboratory-framed average diffusion tensors estimated from the various distribution bins. Brightness indicates the signal fractions corresponding to the 'Big' (row 1), 'Thin' (row 2), and 'Thick' (row 3) bins.

Adapted from[69] under the Creative Commons license (http://creativecommons.org/licenses/by/4.0/)

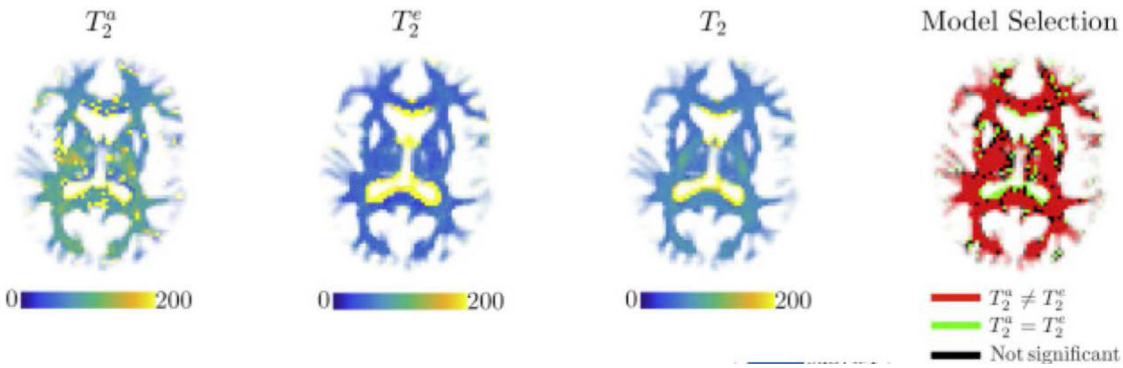

d). There is some debate in the literature, but recent results show that T2 is longer in the more-restricted intra-axonal space in the living human brain.

Adapted from[27] with permission from Elsevier, Copyright 2018.

7.3.3. Improve single-contrast parameter estimation

Reliable estimation of parameters is challenging with the typically low SNR in diffusion NMR and MRI. In order to obtain a good contrast, sufficiently strong diffusion weighting and/or long diffusion time has to be applied, resulting in a decay of the signal and thus SNR. Adding measurements along an independent dimension not only increases the effective SNR[64,79], but can also improves the diffusion estimates.

van Dusschoten et al. (1995)[10] used the difference in T2 relaxation times in apple parenchyma and mung bean seedlings to discriminate diffusion constants. They observed that the errors of the estimated diffusion constants were much smaller than when a multi-component model was fitted to the diffusion data alone. Celik et al. (2013)[80] show that the accuracy of estimates and their stability with respect to noise is markedly improved in general when a second independent dimension is introduced (Figure 7.3a). While this is showcased for T1-T2 correlation, the results are generalisable to diffusion-relaxation correlation.

In the living human brain it has turned out to be challenging to achieve a unique, biophysically plausible solution for a simple two-component model (intra- and extra-axonal space) using diffusion MRI data alone. Specifically, an analysis of this model revealed a *degeneracy* in parameter estimation on data up to moderate diffusion weightings; two biophysically plausible solutions were shown to be equally supported by the data[81]. Several studies[27,35] show that by measuring both diffusion and T2-relaxation, the two compartments can be disentangled with increased confidence, where high b-values further improve the result (Figure 7.3b).

Figure 7.3. Diffusion-relaxometry can improve single-contrast parameter fitting.

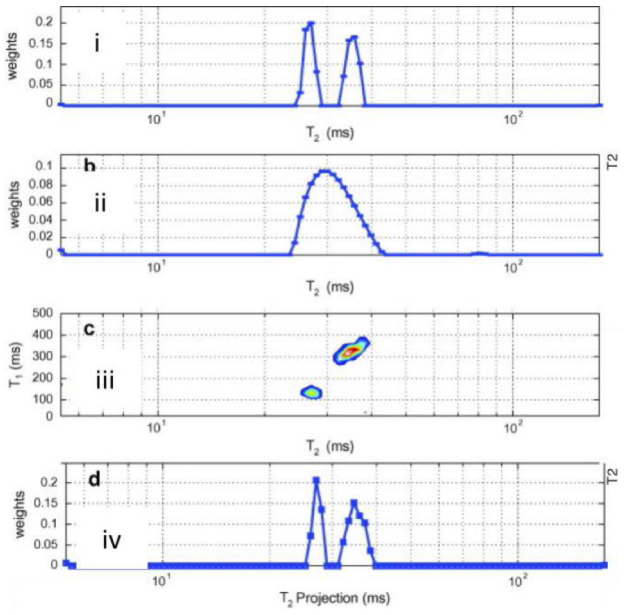

a). Results in a two-component gel, using nonparametric inversion of T1-T2 data (see Section 7.5.1.1). (i) T2 distributions for individual gels combined into a single histogram. (ii) T2 histogram for the two-component sample via inversion, revealing only a single compartment. (iii) T1–T2 histogram for the two-component sample via inversion. (d) T2 projection of the T1–T2 histogram, now revealing both compartments.

Figure adapted from[80] with permission from Elsevier, Copyright 2013.

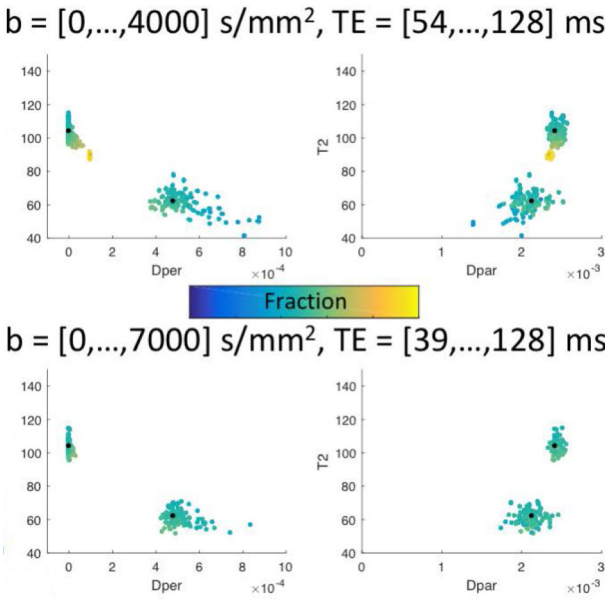

b). Results in a two-component D-T2 simulation of white matter, using model-based estimation (Section 7.5.1.2). The ground truth is indicated by the black dot, and the left and right panel show T2 vs the perpendicular and parallel diffusivity of the modelled tensor, respectively. Including higher b-values reduces the observation of a 'second solution branch' (bottom). T2 in ms, D in mm^2/s.

7.3.4. Weighted signal fractions

Using diffusion NMR alone, multiple studies report signal decays in brain consistent with the presence of intra- vs extra-cellular compartments. However, most of these studies report a discrepancy between the estimated signal fractions and literature values for the volume fractions corresponding to these compartments. Niendorf et al. (1996)[82] argue that a difference in T2 between the intra- and extra-cellular space makes the estimated signal fractions weighted according to their T2, which could cause this discrepancy. Lampinen et al. (2019)[34] report this as a major challenge to estimate the neurite volume fraction, i.e. the fractional voxel volume occupied by neurites. Several studies that combine diffusion and T2 measurements find values that are in better agreement with literature values, e.g.[27,62,83]. However, even if the signal fractions were corrected for relaxation, converting them to volume fractions requires knowledge of the number of detected spins per unit volume in each of the compartments, and this property can be very different for, e.g., myelin, intra- and extra-axonal spaces, and CSF. Claims of measured neurite densities or volume fractions with MRI should therefore be interpreted with caution.

7.4. How to measure diffusion and relaxation simultaneously?

MRI experiments generally consist of an excitation block (commonly a 90° radiofrequency (RF) pulse), a weighting block, and an acquisition/readout block. Here, the aim is to give some intuition as to how different weightings can be used to create diffusion-relaxation correlation experiments, and we refer to Chapter 9 for a more extensive discussion on weightings and readouts. In diffusion MRI, the spin echo (SE) sequence is the most commonly used; diffusion gradients are placed on both sides of the 180° pulse to sensitise the acquisition to diffusion (Fig 4[84]). The SE sequence is simple and elegant, and we will use this as an example of how diffusion and relaxation can be measured simultaneously.

7.4.1. Measuring diffusion and relaxation with the spin-echo sequence

7.4.1.1. A brief recap of the diffusion-gradient spin-echo sequence

The 90° RF pulse will bring the net magnetisation vector in the transverse plane in a given slice, with a fraction of the spins being in phase. From there, the transverse magnetisation component starts precessing around the z-axis with the Larmor frequency. We can write the transverse magnetisation as a complex number that varies over time, with the x-component (sinusoidal) the real and the y-component (cosinusoidal) the imaginary part. The longitudinal magnetisation is zero just after the 90° RF pulse. Due to transverse relaxation effects at different scales (Section 7.2.2), each individual spin will precess with a slightly different frequency, and the dephasing causes the magnitude of the transverse magnetisation to decay.

Then, diffusion weighting is applied by switching on gradients in different directions. Here, a pulsed-gradient is illustrated (the shaded rectangle in Figure 7.4). The gradient causes the total magnetic field to vary spatially: spins precess a bit slower or faster depending on their position. At the end of the gradient waveform, the spins have a position-dependent phase shift (they 'dephased', where we ignore relaxation). After the application of the diffusion gradient, all spins start to precess again with their 'normal' frequency.

At time point TE/2 (with TE the echo time) a 180° pulse is applied, 'flipping' the phase of the spins. This pulse is part of the spin-echo sequence and has now started the correction for reversible transverse dephasing due to chemical shift offset and B0 inhomogeneity. This pulse will yield an echo at time TE, with the signal decay now solely originating from irreversible transverse relaxation. Note that it also inverts the sign of the phase shift caused by the diffusion gradient. The fraction of the longitudinal magnetisation that has grown back will be flipped along the negative axis.

A second diffusion gradient waveform is applied which now tries to undo the phase shift caused by the first gradient. This is the essence of the diffusion encoding: when the molecules remain at the same location the effects of both gradients indeed cancel out, but when these molecules have diffused the effect of the first gradient cannot be undone. The net dephasing of a spin is dependent on its displacement in the direction of the diffusion gradient, and the strength and duration of the gradients. This dephasing of spins will result in a signal drop in addition to the decay from transverse relaxation at time point TE. Just after the echo, the signal will decay again. The longitudinal magnetisation will continue growing until the next 90° RF pulse at the repetition time (TR).

The following sections discuss how relaxation can simultaneously be measured by varying multiple parameters. Here, the classical description as in Eq. 2 will be adopted.

7.4.1.2. Transverse relaxation

From the diffusion-weighted SE sequence it quickly becomes evident that varying the TE will give different T2 weightings to the signal. In the case of a single compartment and fully recovered magnetisation just before the 90° RF pulse (e.g. during the first TR, denoted by S_0), the signal at time TE resulting from transverse relaxation (ignoring diffusion) is

$$S(TE) = S_0 \exp\left(-\frac{TE}{T2}\right). \quad [3]$$

In the case of different compartments, the compartment with the longest T2 will have the largest signal fraction. Various works[27,35,57,61] use pulsed gradient (PG, or Stejskal-Tanner encoding[84]) SE, and vary the TE. When additionally varying the gradient strength and direction, the resulting data will be 4-dimensional in acquisition space (TE,b,θ,ϕ). Others[33,85] additionally vary the waveforms, to generate tensor-valued diffusion encoding (Chapter 3). They limit the acquisitions to axially symmetric b-tensors, with $b_\Delta = (b_{||} - b_\perp)/(b_{||} - 2b_\perp)$ characterising the anisotropy. As such, the acquisition space becomes 5-dimensional (TE,b,b_Δ,θ,ϕ).

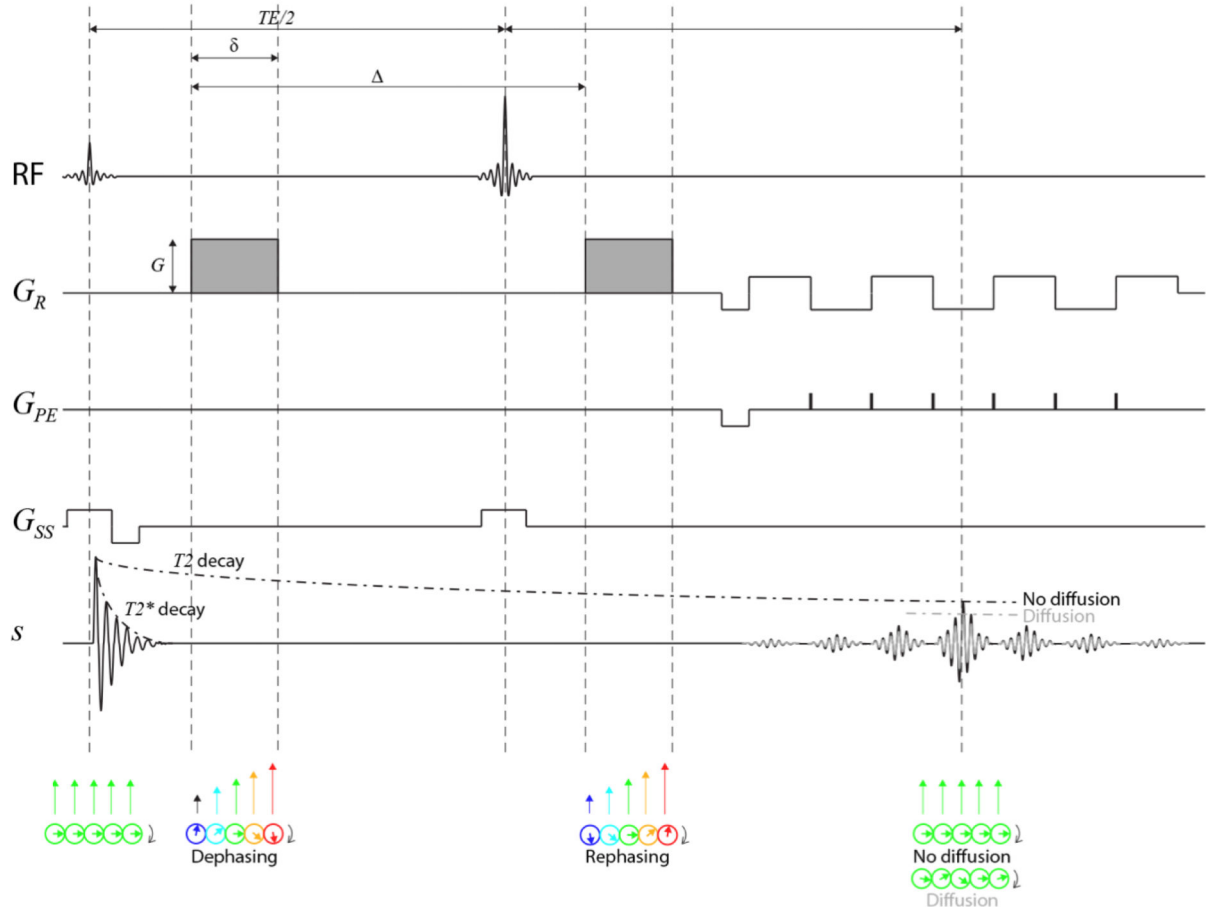

Figure 7.4. The spin-echo sequence can be used for diffusion-relaxation correlation. G_R, G_{PE} and G_S are the readout-, phase-encoding-, and slice-select gradients, respectively. δ and Δ characterise the pulse duration and separation, and G the gradient strength. The coloured arrows schematically represent different the different fields that spins experience due to the gradient being non-zero.

The reversible spin dephasing is completely refocussed in a SE sequence at time TE. Boxerman et al. (1995) and Stables et al. (1998)[86,87] proposed to shift the centre of the acquisition window in time relative to the centre of the spin echo by *delay time* TD, to achieve an 'asymmetric' SE sequence (ASE). In this way, the reversible dephasing contributes to the signal decay. Kleban et al. (2019)[76] combine diffusion PG with ASE to disentangle compartments according to their T2* and frequency difference.

7.4.2.3. Longitudinal relaxation

The T1 weighting can be modulated by varying TR and TE. In the steady state, which occurs during the second TR, the signal at time TE resulting from longitudinal relaxation (again ignoring diffusion) is

$$S(TE,TR) = S_0\left(1-2\exp\left(-\frac{(TR-TE)/2}{T1}\right)+\exp\left(-\frac{TR}{T1}\right)\right)\exp\left(-\frac{TE}{T2}\right). \quad [4]$$

If $TE \ll TR$, then $TR - TE \approx TR$, and Eq. 4 can be further simplified showing that the T1 modulation depends primarily on TR. This strategy to measure T1 is also referred to as saturation recovery (SR) SE; Seland et al. (2005)[59] perform D-T1 correlation experiments using SR-PGSE.

7.4.2. Measuring diffusion-relaxation with variations on the spin-echo sequence and other sequences

Instead of a single 180° pulse and readout per excitation, the Carr-Purcell-Meiboom-Gill (CPMG) sequence applies multiple 180° pulses resulting in multiple echoes. CPMG can greatly speed up acquisition time and can

be placed before the diffusion weighting[53], e.g. to select the T2 range of the water proton magnetisation entering the diffusion measuring sequence, or after diffusion weighting[64]. However, care should be taken regarding spurious echoes and imperfect refocusing. van Dusschoten et al. (1995)[88] use crushers to prevent spurious echoes, whereas Stanisz and Henkelman (1998)[54] use phase cycling. Several works[54,88,89] use short 180 pulse intervals to minimise the effects of diffusion in background gradients (see also Section 7.6.5).

Rather than varying TR to achieve different T1 weightings, Mulkern et al. (2000)[68] incorporate an inversion pulse prior to the 90° pulse in the diffusion-weighted SE sequence for simultaneous D-T1 measurement. The signal attenuation at time TE resulting from relaxation can in that case be written as

$$S(TE,TR,TI) = S_0\left(1-2\exp\left(-\frac{TI}{T1}\right)+\exp\left(-\frac{TR}{T1}\right)\right)\exp\left(-\frac{TE}{T2}\right), \quad [5]$$

with TI the inversion time.

Instead of a single 180° pulse in the SE experiment, a stimulated echo (STE) experiment uses two 90° pulses with a mixing time TM between the pulses; the advantage being that during TM the signal decays with (much slower) T1[90]. This provides avenues to increase the time for diffusion weighting without losing too much signal because of T2, and to inherently add T1 weighting to the signal. However, crushers are needed to eliminate spurious echoes resulting in an SNR penalty. In addition, complications with cross relaxation (magnetization transfer) give an artefactual time-dependence of D for STE sequences when applied to water in biomaterials like brain tissue[41,45,91]. Diffusion-relaxation correlation using STE is adopted in several works[11,85].

7.4.3. Sampling the diffusion-relaxation acquisition space

The strategy of sampling the MRI acquisition parameters can have a big impact on the ability to resolve the relevant information from the data. Relaxation and diffusion phenomena are frequently described by exponential decays (e.g. Eqs. 3 and 4), and the influence of the sampling extent and rate on exponential analyses has been studied for decades[92]. To optimally disentangle different decay rates (e.g. associated to different compartments), the signal should be recorded until it decays into the noise. While a linear spacing of data points seems the most straightforward, other – perhaps less intuitive – sampling schemes have been shown to be able to improve results. Bertero et al. (1984)[93] show that with only 5 'geometrically spaced' data points (i.e. $t_i = t_1 d^{t-1}, i = 1,2,\ldots,N$), the restoration of up to 4 exponential components is improved compared to 32 linearly spaced data points (i.e. $t_i = t_1 d(i-1), i = 1,2,\ldots,N$).

For relaxometry, Weiss et al. (1980)[94] have studied optimal sampling schemes for T1 measurement, and Jones et al. (1996)[95] have applied Cramer-Rao theory to find an optimal set of TEs that minimise the variance of the estimated T2 in case of a single compartment. They find that placing 22% of the sampling points at zero TE and 78% at 1.28 T2 yields the best results. Beaulieu et al. (1998)[53] resample linearly spaced echoes to approximate logarithmic sampling. Even though such non-linear echo spacing has been shown to improve accuracy of T2 estimation, Does and Gore (2000)[96] point out that this may not be appropriate in many situations; imperfect refocusing pulses cause progressive loss of transverse magnetisation and can alternate relative T2 fractions or introduce non-monoexponential T2 behaviour. For diffusion, methods for optimal angular sampling have been introduced[97], as well as strategies for optimal angular and radial sampling (i.e., in the case of different b-values)[98]. More recently, such optimisations have also been investigated for b-tensor encoding[99,100].

However, in the case of diffusion-relaxation correlation, the dimensionality of the MRI-acquisition space further increases and the number of combinations of MRI parameters that can be sampled grows exponentially. There is currently no consensus on the strategy of sampling this high-dimensional space. de Almeida Martins and Topgaard (2018)[85] use a pseudorandom sampling strategy in their NMR experiments, but this is less trivial to set up on a clinical MRI scanner, where TE, TR, and TI are more commonly sampled on a grid[28,32,33,35].

Regardless of the sampling strategy, scan times for multidimensional experiments quickly become prohibitive. For efficient D-T2 NMR in homogenous media, Ahola et al. (2015)[101] propose to encode different diffusion

weightings along one spatial dimension by simultaneous application of a gradient pulse and the refocusing pulse, i.e. the strength of diffusion weighting varies linearly as a function of position. By combining this with a CPMG sequence, the 2D experiment can be performed in a single scan. However, in inhomogeneous samples such as biological tissue other strategies have to be used. Hutter et al. (2018)[28] propose to acquire multiple readouts after a single excitation to perform efficient diffusion-T2* relaxometry, and efficient schemes to sample at multiple TI's (see also Chapter 9).

In addition to scan time, hardware limitations further challenge diffusion-relaxation correlation experiments in humans. In diffusion-T2 experiments, the minimally achievable TE for a given diffusion weighting is generally large: on a typical clinical system the minimal TE is around 110 ms for b = 5000 s/mm^2 (Figure 7.5a). This does not leave much room to disentangle compartments with shorter T2. Using the latest ultra-strong gradient hardware[102,103], the accessible b-TE space becomes much larger. Strong gradients can be leveraged to compute T2 of different compartments in human white matter[35,104]. Combining strong gradients with a shorter image readout, diffusion of short T2 components such as myelin water might become measurable[105,106] (Figure 7.5b).

Figure 7.5. Increase of the accessible parameter space with ultra-strong gradients and shorter readouts.

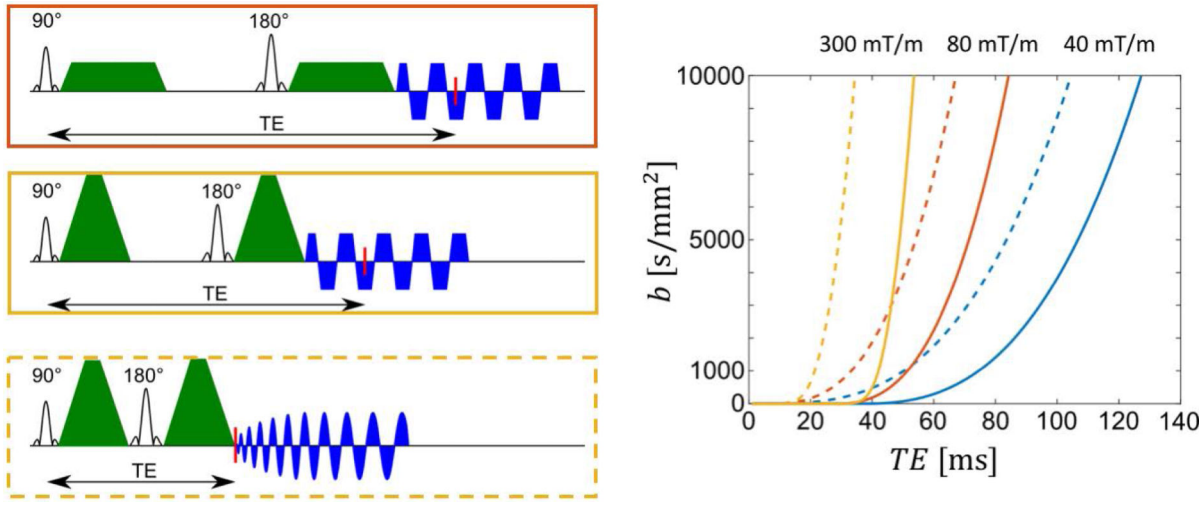

a). b-value vs minimum achievable echo time (TE) for different maximum gradient amplitudes of 40 mT/m, 80 mT/m and 300 mT/m (represented by different colours), and different readouts (represented by different line styles: solid lines EPI readoud and dashed lines spiral readout.

Figure created by Dr. Lars Mueller and partially adapted from[105] with permission from the authors.

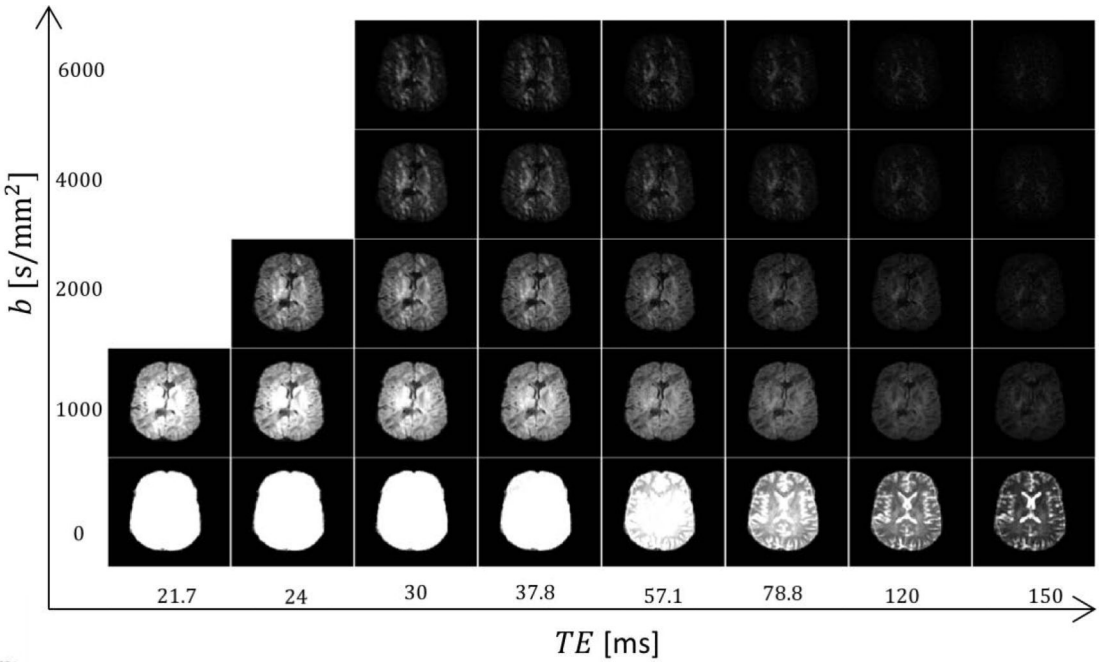

b). With ultra-strong gradients and spiral readout it becomes possible to achieve short TE and high b-values.
Figure adapted from[106] with permission from the authors.

7.5. How to estimate diffusion and relaxation properties?

A heterogeneous material is often described as a sum of microscopic domains that do not exhibit exchange with one another (see Chapter 1). In this framework, each micro-environment is characterised by its diffusion properties (in the absence of restriction/intra-compartmental diffusional kurtosis or at sufficiently low diffusion weightings this can be represented by diffusion tensor $\boldsymbol{D}$, see Chapter 2) and relaxation properties (represented by T1, T2, and T2*, ignoring the frequency offset). The distribution $P(\boldsymbol{D},\mathrm{T1},\mathrm{T2},\mathrm{T2}^*)$ then gives the probability of finding a given $\boldsymbol{D}$,T1,T2 and T2*, and as such characterises the composition of micro-environments within a voxel. The signal can in this case be written as:

$$S(\boldsymbol{B},\mathrm{TR},\mathrm{TE},\mathrm{TD}) = S(0,0,0,0)\int_{\mathrm{Sym}^+(3)}\int_0^\infty\int_0^\infty\int_0^\infty K(\boldsymbol{B},\mathrm{TR},\mathrm{TE},\mathrm{TD},\boldsymbol{D},\mathrm{T1},\mathrm{T2},\mathrm{T2}^*)P(\boldsymbol{D},\mathrm{T1},\mathrm{T2},\mathrm{T2}^*) \quad [6]$$
$$d\mathrm{T1}\,d\mathrm{T2}\,d\mathrm{T2}^*\,\mathrm{d}\boldsymbol{D}.$$

Here, $S(\mathbf{0},0,0,0)$ is the signal when no diffusion- or relaxation-weighting is applied, and $\mathrm{Sym}^+(3)$ denotes the manifold of 3×3 symmetric positive-definite matrices.

The functional form of the kernel K depends on the pulse sequence and the sampling scheme (i.e. which parameters are varied). For the spin-echo experiments without inversion recovery as described in Section 7.4.1, one can derive

$$K(\boldsymbol{B},\mathrm{TR},\mathrm{TD},\mathrm{TE},\boldsymbol{D},\mathrm{T1},\mathrm{T2},\mathrm{T2}^*) = \exp(-\boldsymbol{B}:\boldsymbol{D})\left(1-\exp\left(-\frac{TR}{T1}\right)\right)\exp\left(-\frac{TE}{T2}\right)\exp\left(-\frac{TD}{T2^*}\right). \quad [7]$$

In the equations above, we can recognise the *multi-dimensional Laplace transform* formulation which was first used in the context of NMR in the early 90's[3,107], and only became widely used a decade later[11,12,108]. This formulation was later adapted to accommodate the *distribution of diffusion tensors* rather than diffusivities[109–113], and extended to correlate diffusion tensors with relaxation[85].

7.5.1. The inverse problem

Eq. 6 formulates the forward problem, i.e. given a probability distribution P the resulting signal can be computed. Instead, we are interested in solving the inverse problem: given a set of signals S_n (which can be stored as a as an $N \times 1$ vector $\boldsymbol{s}$ with $n = 1,\ldots,N$) obtained by varying the acquisition parameters, i.e. $(\boldsymbol{B},\mathrm{TR},\mathrm{TE},\mathrm{TD})_n$, find the distribution P. This turns out to be a very hard problem to solve for the formulation above: it requires taking the *inverse Laplace transform*. The inverse Laplace transform is well-known to be ill-posed and ill-conditioned[92]: there is no unique solution[114], and small errors in the initial data can result in much larger errors in the estimates. In contrast, the Fourier transform is well-defined and more easily implemented.

A rich literature exists on solving the inverse Laplace transform, and the approaches can roughly be subdivided according to the priors they impose[115,116]: on the one hand, nonparametric inversion approaches typically do not impose any functional form on P other than that it should be positive and between certain bounds. This can be further extended with priors that promote smoothness and/or sparsity. On the other hand, model-based approaches impose functional forms of P following from a theory about the material, e.g. the number of compartments. Chapters 11 and 12 review these approaches into detail, here they will be briefly introduced and their differences discussed. In addition, we discuss methods that aim to estimate the moments of P.

7.5.1.1. Nonparametric inversion

The nonparametric approach discretises the solution P by *pre-specifying* sets $\boldsymbol{D}_{m_1}, \mathrm{T1}_{m_2}, \mathrm{T2}_{m_3}, \mathrm{T2}^*_{m_4}$ with $m_1 = 1,\ldots,M_1$; $m_2 = 1,\ldots,M_2$; $m_3 = 1,\ldots,M_3$; $m_4 = 1,\ldots,M_4$. The values in these sets are chosen such that they are within plausible bounds for the solution. Then, it aims to estimate the probability of finding pre-specified values of $\boldsymbol{D}_{m_1}, \mathrm{T1}_{m_2}, \mathrm{T2}_{m_3}, \mathrm{T2}^*_{m_4}$, i.e. the discrete fractions $f_{m_1 m_2 m_3 m_4}$ corresponding to *each of the combinations* of $\boldsymbol{D}_{m_1}, \mathrm{T1}_{m_2}, \mathrm{T2}_{m_3}, \mathrm{T2}^*_{m_4}$.

To illustrate this, let us first consider a 1D experiment, i.e. where only TE is varied to estimate T2, and $\boldsymbol{B} = \boldsymbol{0}$, TD = 0, TR $\gg$ T1. In human brain, we would expect the T2 to be somewhere between 10 and 150 ms, so we could for example choose $[\mathrm{T2}_1,\mathrm{T2}_2,\ldots,\mathrm{T2}_{15}] = [10,20,\ldots,150]$ ms. In many applications, however, these values are not chosen to be linearly spaced but instead to be equally spaced in $\ln(\mathrm{R2})$[117] to cover a wide range of decades, without the need to make the number of values M very large. When the fractions f_m (sometimes also referred to as the 'spectral amplitudes' or 'weights' corresponding to each of the $\mathrm{T2}_m$) are stored into an $M \times 1$ column vector $\boldsymbol{f}$ with $m = 1,\ldots,M$, Eq. 6 can be written as:

$$s = \boldsymbol{K} f + \epsilon\,. \qquad [7]$$

Here, $\boldsymbol{K}$ is an $N \times M$ matrix with pre-computed values of the kernel, i.e. $\boldsymbol{K}_{nm} = \exp\left(-\frac{TE_n}{T2_m}\right)$. $\boldsymbol{K}$ is often called the kernel matrix or dictionary. ϵ is an $N \times 1$ column vector representing the experimental error in each measurement (e.g. due to noise). Note that if S is not normalised by $S(0)$, the fractions f_m do not sum up to unity but to $S(0)$.

In a multidimensional experiment, the total number of a priori defined solutions, i.e. the fractions $f_{m_1 m_2 m_3 m_4}$ corresponding to each of the combinations of $\boldsymbol{D}_{m_1}, \mathrm{T1}_{m_2}, \mathrm{T2}_{m_3}, \mathrm{T2}^*_{m_4}$, is $M_1 M_2 M_3 M_4$. For convenient notation, this could be vectorised[1] into an $M \times 1$ column vector $\boldsymbol{f}$ with elements f_m and $m = 1,\ldots,M$ where M =

$M_1M_2M_3M_4$. Here, $\boldsymbol{K}_{nm} = \exp(-\boldsymbol{B}_n : \boldsymbol{D}_m)\left(1 - \exp\left(-\frac{TR_n}{T1_m}\right)\right)\exp\left(-\frac{TE_n}{T2_m}\right)\exp\left(-\frac{TD_n}{T2_m^*}\right)$, and the system of equations can thus be written as Eq. 7. Noticeably, the kernel $\boldsymbol{K}$ quickly becomes enormous. Therefore, nonparametric inversion has mostly been applied in 1D or 2D experiments. Some solutions to deal with large sizes of $\boldsymbol{K}$ have been proposed that either compress K in the 'measurement direction' or in the 'signal predictions direction'.

Regarding compressing the data, a commonly used solution proposed by Venkataramanan and Song[7,108] first consider the sub-kernels $\boldsymbol{K}_i$ of each dimension in case they are separable (e.g. $\boldsymbol{K}_{2,nm} = 1 - \exp\left(-\frac{TR_n}{T1_m}\right)$ and $\boldsymbol{K}_{3,nm} = \exp\left(-\frac{TE_n}{T2_m}\right)$ for T1 and T2, with dimensions $N_2 \times M_2$ and $N_3 \times M_3$ respectively, where N_2 and N_3 denote the number of unique values of TR and TE in the experiment). They then reduce the dimensions by singular value decomposition (SVD). Specifically, SVD is a generalisation of the eigendecomposition and factorises a real matrix as $\boldsymbol{K} = \boldsymbol{U}\boldsymbol{\Sigma}\boldsymbol{V}^T$, where $\boldsymbol{\Sigma}$ is an $N \times M$ matrix with the singular values (non-negative real numbers) on the diagonal in descending order, and $\boldsymbol{U}$ and $\boldsymbol{V}$ are unitary matrices (i.e. $\boldsymbol{U}^T\boldsymbol{U} = \boldsymbol{U}\boldsymbol{U}^T = \boldsymbol{I}$ with $\boldsymbol{I}$ the identity matrix) and have size $N \times N$ and $M \times M$ respectively, with the columns containing the left- and right-singular vectors. By truncating $\boldsymbol{\Sigma}$ to $\widetilde{\Sigma}$ with size $S \times S$ keeping only a subset of the largest singular values, the reduced kernel of size $S \times M$ becomes $\widetilde{K} = \widetilde{\Sigma}\widetilde{V}^T$, where $\widetilde{V}$ is also truncated to have size $M \times S$. Doing this for each sub-kernel, the problem can finally be written as Eq. 7 with $\boldsymbol{K} = \widetilde{K}_2 \otimes \widetilde{K}_3 \in \mathbb{R}^{S_2S_3 \times M_2M_3}$ where $\otimes$ denotes the tensor product. $\boldsymbol{s}$ contains a compressed version of the data, with size $S_2S_3 \times 1$. This is a vectorised version of $\widetilde{S} = \widetilde{U}_1^T S \widetilde{U}_2 \in \mathbb{R}^{S_2 \times S_3}$, where $\widetilde{U}_i$ is truncated to have size $N_i \times S_i$, and $\boldsymbol{S} \in \mathbb{R}^{N_2 \times N_3}$ contains the signal following *each combination* of parameters TR and TE.

While the approach above requires the acquisition of each combination of parameters, a lot of data is immediately thrown away by the SVD compression[118,119]. Acquiring all combinations is time-consuming, and they propose instead to acquire only a few combinations and complete the matrix $\widetilde{S}$ by adopting compressive sensing techniques. Mitchell and Fordham (2011)[120] highlight difficulties with the sub-kernel SVD approach when the kernel $\boldsymbol{K}$ is not separable, and instead propose to compress the data by window averaging: at long TE, for example, all short T2 components have decayed away and the number of data points can be reduced by progressively averaging more data points as TE increases.

Regarding reducing the possible number of solutions, de Almeida Martins and Topgaard (2016)[5] propose to sparsely sample the solution set and perturb the solutions iteratively, so that the size of the kernel in each iteration remains limited. For the diffusion tensors, which theoretically add 6 dimensions to the kernel, they additionally assume axial symmetry so that it can be described by its perpendicular and parallel diffusivity, and two angles defining the first eigenvector ($D_\perp$,$D_{||}$,$\boldsymbol{n}(\theta,\phi)$). Yang et al (2018)[121] implement randomized SVD in which only a single solution at a time is computed to update the SVD process. In addition, they use more coarse dictionaries and obtain intermediate solutions by polynomial fitting.

Once the problem is written in the form of Eq. 7, one could in principle get an estimate $\hat{f}$ by numerically computing the pseuso-inverse $\boldsymbol{K}^+$, for example from SVD as $\boldsymbol{K}^+ = \boldsymbol{V}\boldsymbol{\Sigma}^+\boldsymbol{U}^T$. $\hat{f}$ can then be estimated as

$$\hat{f} = K^+ s\,. \quad [8]$$

1 Vectorisation allows a tensor $\boldsymbol{T}$ of order L and dimensions $J_1, J_2, \ldots, J_L$ with elements $a_{j_1 j_2 \ldots j_L}$ to be interpreted as a vector such that $t = \left[a_{11\ldots1}, a_{21\ldots1}, \ldots, a_{J_1 1\ldots1}, a_{J_1 2\ldots1}, \ldots, a_{J_1 J_2 \ldots J_L}\right]^T = [a_1, a_2, \ldots a_J]$ with $J = J_1, J_2, \ldots, J_L$, i.e. lexicographically ordering the elements.

This formulation solves the problem in the *least-squares* sense: it is equivalent to minimising the sum of squared residuals $\hat{f} = \arg\, min_f \left|\left| s - \boldsymbol{K} f \right|\right|_2^2$. It can be shown that the least-squares estimator is the optimal estimator (in the sense that it has the minimum variance of all estimators) if the experimental errors are uncorrelated and have zero mean and constant variance. For the problem at hand, however, this strategy will not give a very useful answer. The matrix $\boldsymbol{K}$ is ill-conditioned, which means that the inversion process will amplify the errors in $\boldsymbol{S}$ to large errors in $\boldsymbol{f}$. In addition, there exist infinitely many solutions because not each of the columns of $\boldsymbol{K}$ are linearly independent. This can only be ameliorated by making some prior assumptions about $\boldsymbol{f}$ (i.e. *regularisation*), without necessarily imposing a functional form as in model-based approaches.

Lawson and Hanson (1995)[122] imposed a positivity constraint which increases the stability of the solution and coin their algorithm non-negative LS (NNLS). Provencher (1982)[123] in addition proposed to add a regularisation term

$$\hat{f} = \arg\min_f \frac{1}{N} \|s - \boldsymbol{K} f\|_2^2 + \alpha g(f), \quad [9]$$

with g a penalty function and α a regularisation parameter that can be tuned. Several works[115,123] proposed to promote parsimony by employing so-called *Tikhonov regularisation*: a smooth solution with a minimum number of peaks is favoured. In practise, this means that a term is added to the objective function that is a function of the L2-norm of $\boldsymbol{f}$, i.e. $g(f) = \left|\left| \Gamma f \right|\right|_2^2$, with Γ some suitably chosen Thikonov matrix. Daducci et al. (2015)[124] in addition add the L1-norm of $\boldsymbol{f}$, i.e. $\left|\left| f \right|\right|_1^2$ multiplied by a second regularisation parameter β. The L1-norm further promotes sparsity of $\boldsymbol{f}$, i.e. $\boldsymbol{f}$ only having a few non-zero elements, compared to the L2-norm[125], and L1 or L2 regularisation can be adopted depending on the application[4,62,126]. Although regularisation makes the inversion less ill-posed, it might cause bias[127]. Setting the regularisation parameters is generally not trivial[128]; it can either be set empirically or based on simulations, or derived from techniques such as generalised cross-validation[129] or L-curve[130].

Other ways to stabilise the solution have been proposed. Benjamini and Basser (2016)[4] suggest marginal distributions constrained optimisation (MADCO) in which they first estimate the 1D distributions, and then use these to constrain the estimation of the 2D spectrum. They showed that this approach could greatly reduce the amount of data needed. It remains to be evaluated how instabilities and degeneracies in the single-contrast solutions affect this result (see Section 7.3.3). Sun and Dunn (2005)[131] similarly constrained 3D inversion by first solving a 2D inversion (e.g. T1-T2), and then use the resolved spectrum to constrain the remaining inversion (e.g. D-T2). Kim et al. (2017)[61] use the observation that in an imaging experiment, the spectra in neighbouring voxels should be correlated. They adopt spatial regularisation and jointly estimate the parameters for multiple voxels simultaneously rather than for each voxel individually. Alternatives to least-squares minimisation have also be proposed: e.g. maximum entropy inversion[132,133]. de Almeida Martins et al.[69] note that including several B-tensor shapes in the acquisition (as opposed to the conventional Stejskal-Tanner experiment) stabilises the solution.

7.5.1.2. Model-based estimation

A theory about which degrees of freedom have *the most relevant contribution* to the signal allows one to develop a *model*: a concrete realisation of the theory that describes how the signal is related to the relevant degrees of freedom[134]. In contrast, *representations* can be regarded a mathematical means to merely compress or describe the signal. Following this definition, from the inversion procedure discussed in the previous section we obtain a representation of the signal; a distribution of Gaussian signal-contributions. Even if a functional form of this distribution were to be imposed, this would not necessarily be classified as a model according to the definition above if a clear theory is lacking; it might simply be out of convenience.

Here we take a more pragmatic approach and discuss several models and representations that impose a functional form of the distribution P. The continuous distribution fit has shown to be very sensitive to the SNR[10,135], and introducing further priors can significantly stabilise the fit. For example, if the peaks are narrow, imposing delta priors describes the data as well as the continuous distribution, but with fewer parameters. Eqs. 6 and 7 have been at the heart of several techniques in human brain white matter (in the absence of intra-compartmental diffusional kurtosis and exchange); Table 7.1 gives an overview.

Several priors have been proposed for T2 fitting. Does and Gore (2000)[65] consider an SNR per pixel of approximately 30 at the first echo point impractical for nonparametric inversion, and impose delta priors to fit a one-, two-, and three-component slow-exchange model to the data, where an F-test was used to evaluate which model best described each dataset. Stanisz and Henkelman (1998)[54] instead impose a Gaussian prior on the distribution of T2 on the logarithmic scale, because delta priors did not give a statistically correct result.

For diffusion data, a wide range of techniques have been proposed that formulate the signal as resulting from a sum of microenvironments each represented by a tensor[136], and we will discuss a few examples here. Tuch et al. (2002)[137] represent crossing white matter fascicles in the brain by different tensors and fix the diffusivities of the tensors, while they estimate the direction of each fascicle. Behrens et al. (2003)[138] estimate two tensors per voxel; one 'stick' for the axonal compartment with zero perpendicular diffusivity and one 'ball' with similar perpendicular and parallel diffusivity. Zhang et al. (2012)[139] estimate three diffusion tensors (a 'stick' for the intra-axonal compartment, 'zeppelin' with unequal perpendicular and parallel diffusivity for the extra-axonal compartment, and one 'ball' for cerebrospinal fluid), and assume that the first eigenvectors are distributed according to a Watson distribution. They fix the parallel diffusivities and employ a turtuosity assumption for the extra-axonal compartment[140]. Jelescu et al. (2016)[81] investigate the stability of model parameter estimation for the model in Zhang et al. (2012)[139] without the 'ball' compartment, and with free estimation of all the diffusivities. They find a model degeneracy when fitting this model up to moderate b-values; two biophysically plausible solutions fit the data equally well.

Instead of imposing delta priors on diffusivities as in many of the examples described so far, other distributions have been proposed. Lasič et al. (2014)[141] first compute the so-called *powder-average*, which is the averaged signal over all directions, to factor out the dependence of the signal on orientation dispersion. They then propose to model $P(D)$ with a Gamma distribution[142,143]. Scherrer et al. (2016)[113] represent each fascicle by a distribution of tensors, which they parameterise by a matrix-variate Gamma distribution. Interestingly, the concentration parameter in the Gamma distribution can capture the overall compartment's heterogeneity arising from different sources, e.g. orientation dispersion or heterogeneity in underlying diffusivities.

For combined diffusion-relaxation correlation data, early works first try to find evidence for multiple components from a single-contrast, and subsequently obtain estimates for each component in the second dimension. Van Dusschoten et al. (1995)[10] estimate the number m of ensembles, and the signal fraction and corresponding T2 from a CPMG T2 measurement. They then perform $n > m$ PGSE experiments with n different TEs, and estimate n D_{app} values. For each PGSE experiment, the relative amplitude of the m fractions can be calculated given the TE of that experiment and the T2 corresponding to each fraction. Obtaining estimates of the diffusivities for each ensemble then comes down to solving n linear equations with e.g. a SVD routine. Beaulieu et al. (1998)[53] estimates D per TE from a CPMG prepped PGSE sequence, approximating the signal as a monoexponential decay in b.

For the correlation of diffusion tensors and relaxation values, De Santis et al. (2016)[32] first estimate the number and directions of white matter fascicles in each voxel using spherical deconvolution with an a priori defined kernel[150,151]. They then fix the directions and estimate the T1 and diffusivities of the tensor associated with each fascicle, where they further reduce the number of parameters by using the tortuosity assumption. Veraart et al. (2018)[27] reduce the dimensionality of the parameter space by first computing the powder average of the diffusion data per TE, and then jointly fitting a 'stick-zeppelin' with two different T2's to the diffusion and

relaxation data. As in previous work[81] they do not fix diffusivities, and show that adding the T2 dimension has potential to resolve the degeneracy.

Table 7.1. Overview of diffusion, relaxation, and diffusion-relaxation models and representations. Here, the definition of the Delta distribution is $\int_{-\infty}^{\infty}\delta(x-a)f(x)dx = f(a)$ and we abuse the same notation for multivariate distributions, vectors, and tensors; d_i denotes the width of the Gaussian distribution, $\boldsymbol{n} = \boldsymbol{n}(\theta, \phi)$, Γ_p is the multivariate Gamma function, M is a confluent hypergeometric function, and diffusivities are given in $\mu m^2/ms$.

Dimension	Distribution	Example	References
T2	Delta	$P(\mathrm{T2}) = \sum_{\mathrm{i}=1}^{M} f_{\mathrm{i}}\delta(\mathrm{T2}-\mathrm{T2_i})$	65,144
T2	Log-normal	$P(\ln(\mathrm{T2})) = \sum_{\mathrm{i}=1}^{M} \frac{a_i}{\sqrt{\pi}\ln(d_{\mathrm{i}})}\exp\left(-\frac{(\ln(\mathrm{T2})-\ln(\mathrm{T2_i}))^2}{(\ln(d_{\mathrm{i}}))^2}\right)$	54,145
$\boldsymbol{D}$	Delta	$P(D) = \delta(D - D_{app})$	DTI[146]
$D_\perp, D_\parallel, \boldsymbol{n}$	Delta	$P(D_\perp, D_\parallel, n) = \sum_{\mathrm{i}=1}^{M} f_{\mathrm{i}_i}\delta(D_\perp - 0.4, D_\parallel - 1.5, n - n_i)$	Multi-tensor[137]
$D_\perp, D_\parallel, \boldsymbol{n}$	Delta	$P(D_\perp, D_\parallel, n) = f_a\delta(D_\perp, D_\parallel - D_{\parallel,a}, n - n_a) + f_e\delta(D_\perp - D_b, D_\parallel - D_b)$	Ball and stick[138]
$D_\perp, D_\parallel, \boldsymbol{n}$	Delta, Watson	$P(D_\perp, D_\parallel, n) = f_a\delta(D_\perp, D_\parallel - 1.7)M\left(\frac{1}{2}, \frac{3}{2}, \kappa\right)^{-1}\exp\left(\kappa(\mu\cdot n)^2\right) + f_e\delta(D_\perp - 1.7(1-f_a), D_\parallel - 1.7, n-\mu) + f_b\delta(D_\perp - D_b, D_\parallel - D_b)$	NODDI[139]
$D_\perp, D_\parallel, \boldsymbol{n}$	Delta, Watson	$P(D_\perp, D_\parallel, n) = \left(f_a\delta(D_\perp, D_\parallel - D_{\parallel,a}) + f_e\delta(D_\perp - D_{\perp,e}, D_\parallel - D_{\parallel,a})\right)M\left(\frac{1}{2}, \frac{3}{2}, \kappa\right)^{-1}\exp\left(\kappa(\mu\cdot n)^2\right)$	NODDIDA[81]
D	Gamma	$P(D) = D^{\alpha-1}\frac{\exp(-D/\beta)}{\Gamma(\alpha)\beta^\alpha}$	DIVIDE[141,147]
$\boldsymbol{D}$	Matrix-variate Gamma	$P(D) = \sum_{\mathrm{i}=1}^{M} f_{\mathrm{i}}\frac{\lvert D\rvert^{\kappa-2}}{\lvert\Sigma\rvert^\kappa\Gamma_3(\kappa)}\exp\left(-\mathrm{tr}\left(\Sigma^{-1}D\right)\right)$	DIAMOND[113,148]
$\mathrm{T2}, D_\perp, D_\parallel, \boldsymbol{n}$	Delta	$P(\mathrm{T2}, D_\perp, D_\parallel, n) = \left(f_a\delta(\mathrm{T2}-\mathrm{T2}_a, D_\perp, D_\parallel - D_{\parallel,a}) + f_e\delta(\mathrm{T2}-\mathrm{T2}_e, D_\perp - D_{\perp,e}, D_\parallel - D_{\parallel,e})\right)P(n)$	Standard model[27,149]
$\mathrm{T1}, D_\perp, D_\parallel, \boldsymbol{n}$	Delta	$P(\mathrm{T1}, D_\perp, D_\parallel, n) = \sum_{i=1}^{M} f_i\delta(\mathrm{T1}-\mathrm{T1}_i, D_\perp - D_{\parallel,i}(1-f), D_\parallel - D_{\parallel,i}, n - n_i)$	IR-DTI[32]

7.5.1.3. Estimation of moments

The free inversion and model-based estimation approaches typically aim at characterising the distribution P either by imposing some properties (e.g. smoothness) or a functional form. Instead of characterising the distribution itself, several studies have proposed to estimate its moments (or cumulants, which provide an alternative to the moments) as useful descriptors of its shape[152]. The cumulants can be directly estimated from the signal without the need to first estimate P.

In diffusion MRI this strategy is commonly adopted[153,154]. The cumulants are related to the Taylor expansion in b of the logarithm of the signal near $b = 0$, i.e. in 1D:

$$\ln S(b) = \ln S(0) - b\overline{D} - \frac{1}{6}b^2\overline{D}^2K + \cdots \quad [10]$$

Here $\overline{D}$ is the mean of the distribution, and K is the excess kurtosis, related to the variance of the distribution[155]:

$$\overline{D} = \int_0^\infty DP(D)dD \quad [11]$$

$$\mathrm{var}(D) = \int_0^\infty \left(D - \overline{D}\right)^2 P(D)dD \quad [12]$$

$$\mathrm{K} = \frac{3\mathrm{var}(D)}{\overline{D}^2} \quad [13]$$

Diffusion tensor imaging (DTI[146]) considers only the first two terms in Eq. 10, and diffusion kurtosis imaging (DKI[155]) involves the first three terms. It should be noted that the Taylor expansion does not converge for high b in the case of multiple Gaussian compartments (Eq. 7)[153]; the accuracy of the estimates will decrease when the b-values are beyond the *radius of convergence*[156].

Estimation of moments or cumulants has been performed in relaxometry[157] and multidimensional diffusion MRI[112] separately, and very recently also for D-T2 relaxometry data[73].

7.5.2. Uncertainty

Most works report a single solution to the inverse problem; this *point estimate* aims to reflect the "best guess" of the parameter value. Point estimates, however, do not provide any information on the uncertainty or interdependency of parameters. For nonparametric inversion, Prange and Song (2009)[158] aim to capture the uncertainty and estimate an ensemble of solutions using Monte Carlo sampling. Specifically, based on Bayes' rule, they sample from the posterior distribution $P(\boldsymbol{f}|\boldsymbol{s}) \propto P(\boldsymbol{s}|\boldsymbol{f})P(\boldsymbol{f})$, with $P(\boldsymbol{s}|\boldsymbol{f})$ the likelihood function and $P(\boldsymbol{f})$ the prior. The likelihood function contains a formulation for the forward problem, e.g. $\boldsymbol{s} = \boldsymbol{K}\boldsymbol{f}$ as in Eq. 7, and a noise model. Markov Chain Monte Carlo (MCMC) algorithms are commonly used to sample from the posterior distribution. Prange and Song (2009)[158] propose a non-negative multi-normal distribution for the likelihood and a constant prior giving an equal probability to any value of $\boldsymbol{f}$. Upon sampling the posterior distribution of a T2 experiment with an enhanced Gibbs sampler[159], they find an increasingly upward bias in spectral values with decreasing T2, and correlations between spectral positions. Several studies[23,62,69,85] use bootstrap procedures which randomly sub-select data points and compute a spectrum for each subsampling. From this ensemble of solutions, confidence intervals can be estimated and Laplace inversion can be stabilised against spurious peaks in the correlation maps.

For model-based estimation, the principles above have similarly been used to quantify uncertainty and correlations, e.g. using MCMC to sample from the posterior distribution of several microstructural models[138,160–162]. Harms and Roebroeck (2018)[163] provide an efficient GPU-based implementation of MCMC that is compatible with a wide range of models. Alternatively, several works[164–166] use bootstrapping to characterise uncertainty in diffusion MRI estimation. Such estimates of uncertainty have been integrated in

tractography for the virtual reconstruction of fibre pathways: probabilistic tractography - as opposed to deterministic tractography - aims to take into account the uncertainty of the fiber direction estimate in each voxel.

7.5.3. Laplace vs Fourier

In addition to the Laplace transform in Eq. 6, the *Fourier transform* is used for multi-dimensional experiments involving diffusion as well; an excellent overview is given in Callaghan (2011)[1]. In a 1D diffusion NMR experiment with narrow pulses, the Fourier transformation with respect to q (with $q = \gamma\delta G$ where γ is the gyromagnetic ratio, δ is the pulse duration, and G is the gradient strength) gives the *spectrum of displacements*[167,168]. For Gaussian diffusion with diffusion coefficient D, this spectrum is a Gaussian function with width D. In the case of multiple microenvironments, each environment i would exhibit a Gaussian spectrum with width D_i, and the overall spectrum would be a superposition. This spectrum would be very hard to disentangle, and as such the *spectrum of diffusion coefficients* $P(D)$ (or $P(\boldsymbol{D})$ in the case of the distribution of tensors in Eq. 6) might be more intuitive to work with.

Several studies report combined Laplace- and Fourier transformation in diffusion-relaxation correlation. Britton et al. (2004)[169] correlate T2 with molecular displacement in water diffusing through an alginate bead pack. They performed Fourier transformation to obtain a propagator for each TE, and inverse Laplace transformation for each displacement in the propagator. Washburn and Callaghan (2007)[170] perform diffusion T2-T2 exchange experiments and combine a Fourier dimension with two inverse Laplace dimensions. As such, they can better determine whether changes in T2 comes from intra- or inter-pore transport, as they have access to the displacement of spins.

7.6. How to validate diffusion-relaxation correlation?

Eq. 6 in the previous section was presented as an overarching framework of methods that describe materials as a sum of microscopic domains that are each already fully *coarse grained*, which means that the diffusion time is long enough for the water molecules to have already homogenised intra-compartmental microstructure, and are not in exchange. If these assumptions are invalidated, estimates from inversion- or model-based analysis could become biased and/or meaningless. In this Section, we briefly discuss strategies that have been used to validate and evaluate results from diffusion-relaxation measurements (for a more general overview see e.g. [171,172] and references therein), and hallmarks that could point to invalid assumptions. Specifically, we will discuss 1) computer simulations, 2) phantoms, 3) histology, 4) adjusting the measurement regime, and 5) adding MRI dimensions. Chapters 13 and 14 consider validation into more detail.

7.6.1. Computer simulations

With the development of improved computational hardware, computer simulations have become an important tool to predict and validate MR measurements. Assuming a ground truth, forward simulation of Eq. 6 is commonly used to evaluate precision and accuracy of the inversion[63,173]. For more complex scenarios, such as the presence of restrictions, various approaches have been developed. Some rely on the evaluation of Fick's second law of diffusion; given a geometry, this partial differential equation can be solved analytically for a limited range of initial- and boundary conditions, or numerically for more general configurations. Brownstein and Tarr (1979)[174] and Callaghan (1995)[175] derived expressions for relaxation- and PGSE experiments respectively, in planar, cylindrical, and spherical pores under conditions of surface relaxation based on the eigenmode expansion of the propagator. This was also extended to general waveforms by breaking the waveform into intervals and writing a propagator for each interval[176–179]. Using this framework, Callaghan et al. (2003)[180] simulated T2-D signals from restricted geometries (plane and sphere) with varying size and wall relaxivities, and study the 2D Laplace inversion spectra[7]. The spectra showed, in addition to the primary mode, a wide spread of diffusion and relaxation values even for these simple pores (Figure 7.6a)[181]. These extra features

might prove of value to separate surface- from bulk fluid in the pore. Novikov et al. (1998)[182] developed a 1D numerical model of restricted diffusion and relaxation in multi-compartment planar geometries for PG CPMG, and this was later extended to cylindrical geometries[183].

Other approaches perform Monte Carlo simulations of the movements of a large number of hypothetical molecules. These approaches are becoming increasingly popular because of their greater flexibility to model arbitrary configurations and multiple processes simultaneously (e.g. diffusion, exchange, susceptibility, and relaxation). For example, Lin et al. (2018)[70] simulate myelinated axons with different T2 in each compartment, and diffusing molecules can exchange between compartments with a probability according to a pre-defined axonal membrane permeability (Figure 7.6b). Ruh et al. (2018)[50] use Monte Carlo simulations to study diffusion in microenvironments with heterogeneous susceptibility.

Figure 7.6. Computer simulations in diffusion-relaxation correlation.

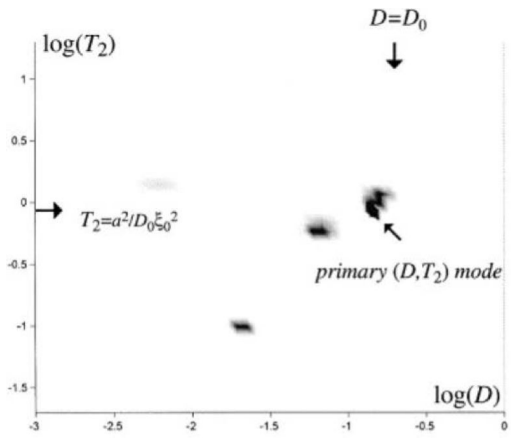

a). Simulation of a simple planar restricted geometry with wall relaxation gives complex features in a D-T2 plot. The diagonal arrow indicates the position of the primary relaxation–diffusion mode obtained from the low-q data.

Figure adapted from[180] with permission from Elsevier, Copyright 2003.

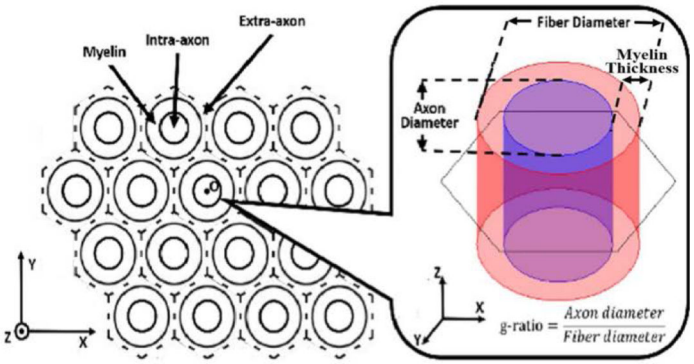

b). Monte Carlo simulation geometry of myelinated axons in a periodic array of hexagonal columns, each axon is surrounded by a permeable myelin sheath.

Figure adapted from[70] with permission from John Wiley and Sons, Copyright 2018.

7.6.2. Phantoms

Phantoms to validate diffusion-relaxation correlation have a well-characterised composition and are usually man-made and non-biological, although food phantoms have also been used (Chapter 13). Realistic phantoms

typically contain an NMR visible liquid with similar diffusion coefficient and relaxation times as can be found in the material of interest, and an NMR invisible material that reflects realistic architectural configurations, e.g. intra- and extra-axonal spaces and/or crossing fibres for white matter. Regarding NMR-visible liquids, several examples can be found in literature to validate multi-dimensional MR experiments, e.g. to evaluate strategies for faster acquisition and analysis against conventional methods. Benjamini and Basser (2016, 2018)[4,126] used doped water and polyvinylpyrrolidone (PVP) to create T1-D phantoms with distinct peaks, which were characterised individually in advance. Ahola et al. (2015)[101] use porous silica gel powder immersed in water to create D-T2 spectra from water in the pores and between the particles. Dairy cream has been used as a phantom that has both bi-exponential diffusion as well as T2[16,184].

Regarding the architectural configuration, careful thought should be given to the dimensions, surface relaxation, and susceptibility effects of the material in which the liquid will reside. de Almeida Martins and Topgaard (2018)[85] combine a liquid crystal exhibiting anisotropy[185] with a yeast suspension composed of microscopic spherical cells with intra- and extra-cellular isotropic diffusion of different magnitudes. They use this to evaluate 6-dimensional T1-T2-**D** inversion (Figure 7.7).

7.6.3. Histology

Histology can be used to study the microscopic anatomy of biological tissues and thus provides an independent window into the composition. Tissues are typically fixed to preserve their structure and then embedded in a medium. Sections of the tissue can then be stained to give contrast to the tissue and highlight specific structures or chemical components. Benjamini and Basser (2017)[62] used immunohistochemistry to mark astrocytes, microglia, myelin oligodendrocyte glycoprotein, and neurofilaments with antibodies, in sections of a rat spinal cord. They then correlated properties of T2-D derived components to the relevant immunohistochemistry features. Although this cannot be used as an absolute "ground truth" for MRI-derived measures because of differences in the source of the signal and changes after fixation and embedding, it can provide useful independent information (Chapter 14).

7.6.4. Adjusting the measurement regime

Modelling all the compartments in a material typically involves the estimation of a relatively large number of parameters. If prior knowledge exists on differences in diffusion- and/or relaxation properties between components, the experiment can be set up to 'filter out' certain compartments while keeping others. This might facilitate the fitting and rule out errors from the inversion procedure; the results from the full- and filtered experiment should at least be compatible. Sørland et al. (2004)[13] used this principle in a T2-D experiment of crude oil and water in rock cores, where they apply sufficiently high diffusion gradients to filter out the signal from water and study the T2 decay of oil. McKinnon and Jensen (2019)[31] and Kleban et al. (2019)[76] used high diffusion-weightings to sufficiently decay the signal from extra-axonal water and study the T2 and T2* from intra-axonal water, respectively. Tax et al.[186] used high b-values and isotropic diffusion weighting to filter out compartments in which water can move at least in one direction, thereby targeting small spherical compartments such as cell bodies. Andrews et al. (2006)[56] targeted myelin water by using an inversion pulse with suitable TI to nullify signal from the intra- and extra-axonal spaces in excised frog sciatic nerve. They then measure diffusion and T2 from the remaining compartment, and compare this to measurements that are sensitive to all compartments simultaneously.

7.6.5. Adding MRI dimensions

Apart from diffusion and relaxation, other phenomena play a role at the time scale of typical measurements. For example, exchange between compartments can affect the observed fractions[187], and mesoscopic field gradients can bias the estimated relaxation rates. The influence of these effects might be estimated with additional MRI measurements, effectively adding dimensions beyond diffusion and relaxation. To measure exchange, the same

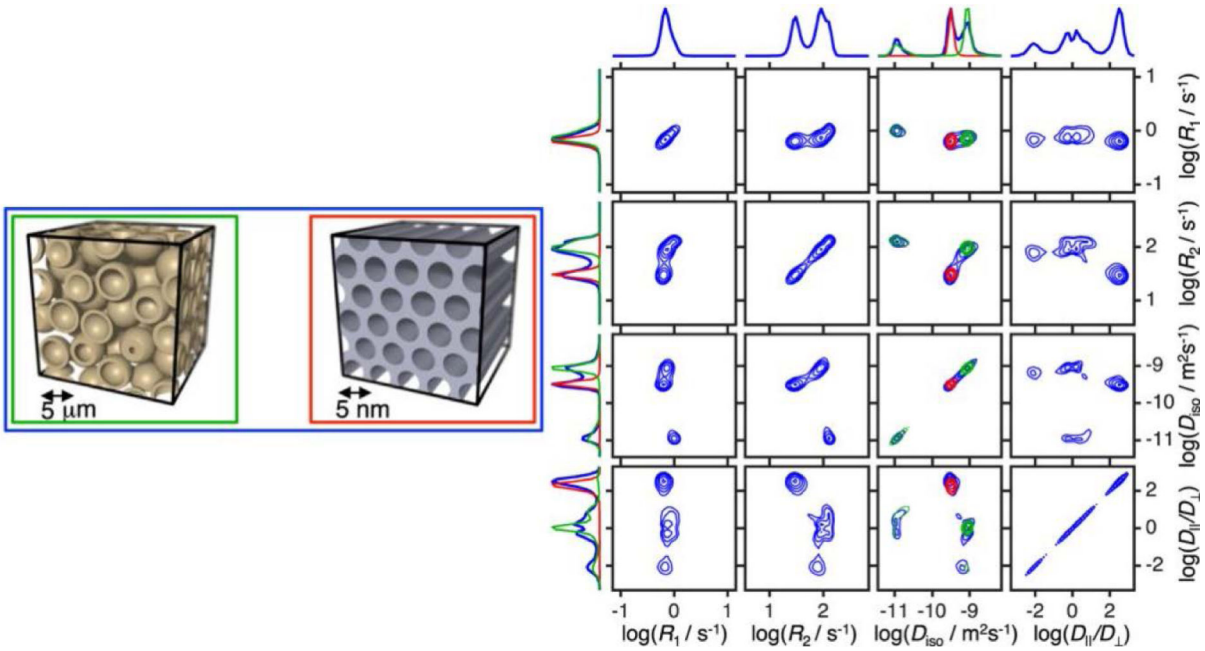

Figure 7.7. Phantoms for diffusion-relaxation correlation. This phantom is composed of a yeast suspension microstructure (green frame, set of spherical shells representing the cell membranes that delimit the intra- and extracellular domains), and a liquid crystal microdomain (red frame, coherent set of cylindrical water channels in a continuous matrix of detergent and hydrocarbon. The blue frame demarks the entire sample volume. Six dimensional $P(R1, R2, D_{iso}, D_{||}/D_{\perp}, \theta, \phi)$ distribution calculated through unconstrained inversion of data acquired with the phantom.

property (e.g. relaxation or diffusion) has to be encoded at two different times[188,189]. If exchange takes place during the mixing time, the spectra will reveal peaks located off the diagonal. Chapter 5 considers exchange experiments into more detail.

Regarding local internal magnetic field gradients, Carr and Purcell (1954)[49] showed that the sensitivity of the measurement to the additional dephasing is dependent on the time between echoes in a CPMG sequence; shorter durations result in less echo attenuation. By incorporating a dimension in which this timing is varied, the local field can potentially be estimated. Seland et al. (2004)[18] perform D-T2 experiments with an extra dimension for internal gradients in liquid-saturated packings of glass beads and perform Laplace inversion to disentangle the different phenomena.

7.7. Summary and Discussion

This Chapter has focused on combining diffusion and relaxation MR to study the heterogeneity of biological tissue. It should be apparent that relaxometry provides rich information that can complement the information obtained from studying the diffusion process. To date this has been mostly applied in excised tissue and animal imaging, but more recently diffusion-relaxation correlation has also found its way into in-vivo human imaging. Improvements in MRI hardware and imaging strategies, such as strong gradients, multi-band imaging, and efficient image readouts, have greatly facilitated this translation, but challenges remain that currently hamper its widespread adoption. In the next Sections, we will discuss some of the challenges and limitations, and provide an outlook for the use of diffusion-relaxation correlation in clinical applications.

7.7.1. Challenges and limitations

A first limitation is noise. The signal should be measured until it has almost completely decayed, ideally by at least three orders of magnitude before it reaches the noise floor[128]. This would correspond to an SNR of at least 1000, which is much higher than what is commonly achieved in in-vivo human imaging. This might to some extent be addressed by averaging multiple acquisitions, but this is in turn challenged by the limited acquisition time. Denoising techniques have been developed for MR images and for diffusion MRI specifically (e.g. [190,191]), but care should be taken that no relevant information is removed from the images. In addition to the presence of noise, the distribution of the noise can further challenge accurate estimation. The noise in MRI magnitude images are not Gaussian distributed; they can be Rician distributed or non-central Chi distributed, with stationary or non-stationary noise, depending on the combination of the coils and parallel imaging techniques used[192]. The commonly used least-squares formulation can give biased results in this case. Nevertheless, promising results have been shown in in-vivo human data where the problem was sufficiently constrained, e.g. in model-based approaches[27,106], in 2D inversion approaches[75], and in higher dimensional inversion approaches with multidimensional diffusion[33]

Establishing reasonable assumptions is another major challenge. Model-based approaches commonly rely on a theory (i.e. a 'picture' of what the reality might look like). Based on this, assumptions on the relevant degrees of freedom might be derived, for example diffusion in white matter is commonly modelled with two compartments. However, if such a theory is not available (e.g. in disease), an interplay between modelling and nonparametric inversion could provide a useful strategy to find suitable constraints. As inversion strategies have been so commonly used in NMR of porous media over the years, common artefacts are well-recognised and hallmarks of invalid assumptions can sometimes be derived from the spectra. For example, 'pearling' in which local islands of peaks arise, is well-known to be an artefact of the transformation[1]. An example of a hallmark is when both T1 and T2 are part of the multi-dimensional experiment, exchange can dislocate peaks and add additional ones that may have negative amplitudes incompatible with the positivity constraint[193]. Restricted diffusion and wall-relaxation may also exhibit specific hallmarks[180]. Once suitable constraints have been established, a more accurate quantification could be obtained by fitting the compartmental model rather than reading the values from the spectra[194].

Perhaps the most challenging aspect of translating diffusion-relaxation correlation to in-vivo human imaging is the acquisition and the long measurement times associated with it. MR fingerprinting uses very fast acquisitions and relies on a large amount of lower quality images to derive the fingerprint[51]. Other ways of fast acquisition are discussed in Chapter 9. Alternatively, combining compressive sensing techniques with sparse acquisitions can reduce the number of necessary data points. Finally, some practical challenges may complicate acquisition; commercially available diffusion sequences do not always allow to change TE and diffusion time independently, which unintentionally mixes these experimental dimension[27]. Also setting up acquisitions with many different TEs and TRs can be cumbersome and require careful bookkeeping.

7.7.2. Outlook

Diffusion-relaxometry has the potential to provide a more complete picture of tissue microstructure than their 1D counterparts. In clinical applications, the increased sensitivity and specificity to changes in tissue microstructure can result in improved disease monitoring and diagnosis. This links in with the trend of personalised medicine, in which the treatment is tailored to the specific characteristics of each individual. Preliminary applications in different organs, such as brain, prostate, and placenta, have shown that the potential usefulness of this technique is widespread. Moving forward, diffusion-relaxation correlation can further be extended in terms of dimensions; it is well-known that T2* in white matter is anisotropic and thus depends on the orientation of the tissue with respect to the main magnetic field, and recent studies also show T2 anisotropy[31,195]. If different rotations of the tissue in the scanner are feasible, T2*- and T2 tensors can thus

potentially be estimated. Finally, data-driven and machine learning methods provide exciting new avenues to analyse the high-dimensional data in diffusion-relaxation correlation[196].

Acknowledgements

CMWT is supported by a Rubicon grant (680-50-1527) from the Netherlands Organisation for Scientific Research (NWO) and a Sir Henry Wellcome Fellowship (215944/Z/19/Z). The author is grateful to Dr. Lars Mueller for his contributions to Fig. 7.5.

References

1. P. T. Callaghan, *Translational dynamics and magnetic resonance : principles of pulsed gradient spin echo NMR*, Oxford University Press, 2011.
2. H. Peemoeller, R. . Shenoy and M. . Pintar, *J. Magn. Reson.*, 1981, **45**, 193–204.
3. A. E. English, K. P. Whittall, M. L. G. Joy and R. M. Henkelman, *Magn. Reson. Med.*, 1991, **22**, 425–434. PubMed PMID: 1812377.
4. D. Benjamini and P. J. Basser, *J. Magn. Reson.*, 2016, **271**, 40–45. PubMed PMID: 27543810.
5. J. P. de Almeida Martins and D. Topgaard, *Phys. Rev. Lett.*, 2016, **116**, 087601. PubMed PMID: 26967442.
6. É. Chouzenoux, S. Moussaoui, J. Idier and F. Mariette, *IEEE Trans. Signal Process.*, 2010, **58**, 6040–6051.
7. L. Venkataramanan, Y. Q. Song and M. D. Hürlimann, *IEEE Trans. Signal Process.*, 2002, **50**, 1017–1026.
8. G. Lindblom, H. Wennerstrom and G. Arvidson, *Int J Quantum Chem*, 1977, **12**, 153–158.
9. W. Heink, J. Kärger and H. Pfeifer, *ZEITSCHRIFT FUR Phys. CHEMIE-INTERNATIONAL J. Res. Phys. Chem. Chem. Phys.*, 1991, **170**, 199–206.
10. D. van Dusschoten, P. A. de Jager and H. van As, *J. Magn. Reson. Ser. A*, 1995, **116**, 22–28.
11. M. . Hürlimann and L. Venkataramanan, *J. Magn. Reson.*, 2002, **157**, 31–42. PubMed PMID: 12202130.
12. M. D. Hürlimann, L. Venkataramanan and C. Flaum, *J. Chem. Phys.*, 2002, **117**, 10223–10232.
13. G. H. Sørland, H. W. Anthonsen, J. G. Seland, F. Antonsen, H. C. Widerøe and J. Krane, *Appl. Magn. Reson.*, 2004, **26**, 417–425.
14. G. Maddinelli and E. Peron, *Appl. Magn. Reson.*, 2005, **29**, 549–559.
15. S. Godefroy and P. T. Callaghan, *Magn. Reson. Imaging*, 2003, **21**, 381–383. PubMed PMID: 12850739.
16. M. D. Hürlimann, L. Burcaw and Y.-Q. Song, *J. Colloid Interface Sci.*, 2006, **297**, 303–311. PubMed PMID: 16300777.
17. P. T. Callaghan, S. Godefroy and B. N. Ryland, *Magn. Reson. Imaging*, 2003, 21, 243–248. PubMed PMID: 12850714.
18. J. G. Seland, K. E. Washburn, H. W. Anthonsen and J. Krane, *Phys. Rev. E*, 2004, **70**, 051305.
19. Y. Zhang and B. Blümich, *J. Magn. Reson.*, 2014, **242**, 41–48. PubMed PMID: 24607821.
20. Y. Qiao, P. Galvosas, T. Adalsteinsson, M. Schönhoff and P. T. Callaghan, *J. Chem. Phys.*, 2005, **122**, 214912. PubMed PMID: 15974795.
21. M. D. Hürlimann, *Appl. Magn. Reson.*, 2004, **25**, 651–660.
22. D. E. Freed and M. D. Hürlimann, *Comptes Rendus Phys.*, 2010, **11**, 181–191.
23. D. W. de Kort, J. P. M. van Duynhoven, F. J. M. Hoeben, H. M. Janssen and H. Van As, *Anal. Chem.*, 2014, **86**, 9229–9235. PubMed PMID: 25141338.
24. Y. Qiao, P. Galvosas and P. T. Callaghan, *Biophys. J.*, 2005, **89**, 2899–2905. PubMed PMID: 16100271.
25. N. Marigheto, L. Venturi and B. Hills, *Postharvest Biol. Technol.*, 2008, **48**, 331–340.
26. S. Eriksson, K. Elbing, O. Söderman, K. Lindkvist-Petersson, D. Topgaard and S. Lasič, *PLoS One*, 2017, **12**, e0177273. PubMed PMID: 28493928.
27. J. Veraart, D. S. Novikov and E. Fieremans, *Neuroimage*, 2018, **182**, 360–369. PubMed PMID: 28935239.
28. J. Hutter, P. J. Slator, D. Christiaens, R. P. A. G. Teixeira, T. Roberts, L. Jackson, A. N. Price, S. Malik and J. V. Hajnal, *Sci. Rep.*, 2018, **8**, 15138. PubMed PMID: 30310108.

29. P. J. Slator, J. Hutter, M. Palombo, L. H. Jackson, A. Ho, E. Panagiotaki, L. C. Chappell, M. A. Rutherford, J. V. Hajnal and D. C. Alexander, *Magn. Reson. Med.*, 2019, **82**, 95–106. PubMed PMID: 30883915.
30. M. Pizzolato, E. J. Canales-Rodríguez, A. Daducci and J.-P. Thiran, *ISMRM*, 2018, 3118.
31. E. T. McKinnon and J. H. Jensen, *Magn. Reson. Med.*, 2019, **81**, 2985–2994. PubMed PMID: 30506959.
32. S. De Santis, Y. Assaf, B. Jeurissen, D. K. Jones and A. Roebroeck, *Neuroimage*, 2016, **141**, 133–142. PubMed PMID: 27444568.
33. C. M. W. Tax, J. P. de Almeida Martins, F. Szczepankiewicz, C. F. Westin, M. Chamberland, D. Topgaard and D. K. Jones, in *ISMRM*, 2018, p. 1101.
34. B. Lampinen, F. Szczepankiewicz, M. Novén, D. van Westen, O. Hansson, E. Englund, J. Mårtensson, C.-F. Westin and M. Nilsson, *Hum. Brain Mapp.*, , DOI:10.1002/hbm.24542.
35. C. M. W. Tax, U. S. Rudrapatna, T. Witzel and D. K. Jones, in *ISMRM*, 2017, p. 0838.
36. N. P. Jerome, J. A. D'Arcy, T. Feiweier, D. M. Koh, M. O. Leach, D. J. Collins and M. R. Orton, *Phys. Med. Biol.*, 2016, **61**, N667–N680. PubMed PMID: 27893459.
37. A. Melbourne, R. Aughwane, M. Sokolska, D. Owen, G. Kendall, D. Flouri, A. Bainbridge, D. Atkinson, J. Deprest, T. Vercauteren, A. David and S. Ourselin, *Magn. Reson. Med.*, 2019, **81**, 350–361. PubMed PMID: 30239036.
38. A. Rydhög, O. Pasternak, F. Ståhlberg, A. Ahlgren, L. Knutsson and R. Wirestam, *Eur. J. Radiol. Open*, 2019, **6**, 198–205. PubMed PMID: 31193664.
39. J. Kowalewski and L. Mäler, *Nuclear spin relaxation in liquids : theory, experiments, and applications*, CRC Press, Taylor & Francis Group, 2nd edn., 2018.
40. M. D. Does, *Neuroimage*, 2018, **182**, 136–148. PubMed PMID: 29305163.
41. T. A. Bjarnason, I. M. Vavasour, C. L. L. Chia and A. L. MacKay, *Magn. Reson. Med.*, 2005, **54**, 1072–1081. PubMed PMID: 16200557.
42. B. Halle, *Magn. Reson. Med.*, 2006, **56**, 60–72. PubMed PMID: 16732594.
43. B. P. Hills, C. Cano and P. S. Belton, *Macromolecules*, 1991, **24**, 2944–2950.
44. N. Bloembergen, E. M. Purcell and R. V. Pound, *Phys. Rev.*, 1948, **73**, 679–712.
45. H. T. Edzes and E. T. Samulski, *J. Magn. Reson.*, 1978, **31**, 207–229.
46. R. L. Kleinberg, W. E. Kenyon and P. P. Mitra, *J. Magn. Reson. Ser. A*, 1994, **108**, 206–214.
47. R. . Kleinberg and M. . Horsfield, *J. Magn. Reson.*, 1990, **88**, 9–19.
48. W. Oakden and G. J. Stanisz, *NMR Biomed.*, 2014, **27**, 672–680. PubMed PMID: 24700546.
49. H. Y. Carr and E. M. Purcell, *Phys. Rev.*, , DOI:10.1103/PhysRev.94.630.
50. A. Ruh, H. Scherer and V. G. Kiselev, *Magn. Reson. Med.*, 2018, **79**, 1101–1110. PubMed PMID: 28524556.
51. D. Ma, V. Gulani, N. Seiberlich, K. Liu, J. L. Sunshine, J. L. Duerk and M. A. Griswold, *Nature*, 2013, **495**, 187–92. PubMed PMID: 23486058.
52. A. C. Yu, C. Badve, L. E. Ponsky, S. Pahwa, S. Dastmalchian, M. Rogers, Y. Jiang, S. Margevicius, M. Schluchter, W. Tabayoyong, R. Abouassaly, D. McGivney, M. A. Griswold and V. Gulani, *Radiology*, 2017, **283**, 729–738. PubMed PMID: 28187264.
53. C. Beaulieu, F. R. Fenrich and P. S. Allen, *Magn. Reson. Imaging*, 1998, **16**, 1201–1210. PubMed PMID: 9858277.
54. G. J. Stanisz and R. M. Henkelman, *Magn. Reson. Med.*, 1998, **40**, 405–410. PubMed PMID: 9727943.
55. S. Peled, D. G. Cory, S. A. Raymond, D. A. Kirschner and F. A. Jolesz, *Magn. Reson. Med.*, 1999, **42**, 911–918. PubMed PMID: 10542350.
56. T. J. Andrews, M. T. Osborne and M. D. Does, *Magn. Reson. Med.*, 2006, **56**, 381–385. PubMed PMID: 16767712.
57. J. Pfeuffer, S. Bröer, A. Bröer, M. Lechte, U. Flögel and D. Leibfritz, *Biochim. Biophys. Acta - Mol. Cell Res.*, 1998, **1448**, 27–36.
58. J. G. Li, G. J. Stanisz and R. M. Henkelman, *Magn. Reson. Med.*, 1998, **40**, 79–88. PubMed PMID: 9660557.
59. J. G. Seland, M. Bruvold, H. Anthonsen, H. Brurok, W. Nordhøy, P. Jynge and J. Krane, *Magn. Reson. Imaging*, 2005, **23**, 353–354. PubMed PMID: 15833645.

60. S. E. Mailhiot, F. Zong, J. E. Maneval, R. K. June, P. Galvosas and J. D. Seymour, *J. Magn. Reson.*, 2018, **287**, 82–90. PubMed PMID: 29306110.
61. D. Kim, E. K. Doyle, J. L. Wisnowski, J. H. Kim and J. P. Haldar, 2017, **78**, 2236–2249.
62. D. Benjamini and P. J. Basser, *Neuroimage*, 2017, **163**, 183–196. PubMed PMID: 28943412.
63. S. De Santis, D. Barazany, D. K. Jones and Y. Assaf, *Magn. Reson. Med.*, 2016, **75**, 372–80. PubMed PMID: 25735538.
64. D. van Dusschoten, C. T. W. Moonen, P. A. de Jager and H. van As, *Magn. Reson. Med.*, 1996, **36**, 907–913. PubMed PMID: 8946356.
65. M. D. Does and J. C. Gore, *Magn. Reson. Med.*, 2000, **43**, 837–844. PubMed PMID: 10861878.
66. W. Qin, C. Shui Yu, F. Zhang, X. Y. Du, H. Jiang, Y. Xia Yan and K. Cheng Li, *Magn. Reson. Med.*, 2009, **61**, 755–760. PubMed PMID: 19191286.
67. S. De Santis, Y. Assaf and D. K. Jones, in *ISMRM*, 2016, p. 1998.
68. R. V. Mulkern, H. P. Zengingonul, R. L. Robertson, P. Bogner, K. H. Zou, H. Gudbjartsson, C. R. G. Guttmann, D. Holtzman, W. Kyriakos, F. A. Jolesz and S. E. Maier, *Magn. Reson. Med.*, 2000, **44**, 292–300. PubMed PMID: 10918329.
69. J. P. de Almeida Martins, C. M. W. Tax, F. Szczepankiewicz, D. K. Jones, C.-F. Westin and D. Topgaard, *Magn. Reson. Discuss.*, 2019, 1–23.
70. M. Lin, H. He, Q. Tong, Q. Ding, X. Yan, T. Feiweier and J. Zhong, *Magn. Reson. Med.*, 2018, **79**, 1650–1660. PubMed PMID: 28656631.
71. M. J. Knight, S. Dillon, L. Jarutyte and R. A. Kauppinen, *Biophys. J.*, 2017, **112**, 1517–1528. PubMed PMID: 28402893.
72. R. Gil, D. Khabipova, M. Zwiers, T. Hilbert, T. Kober and J. P. Marques, *NMR Biomed.*, 2016, **29**, 1780–1790. PubMed PMID: 27809376.
73. L. Ning, B. Gagoski, F. Szczepankiewicz, C.-F. Westin and Y. Rathi, *bioRxiv*, 2019, 598375.
74. G. Lemberskiy, E. Fieremans, J. Veraart, F.-M. Deng, A. B. Rosenkrantz and D. S. Novikov, *Front. Phys.*, , DOI:10.3389/fphy.2018.00091.
75. P. J. Slator, J. Hutter, M. Palombo, L. H. Jackson, E. Panagiotaki, A. Ho, L. C. Chappell, M. A. Rutherford, J. V. Hajnal and D. C. Alexander, in *ISMRM*, 2019, p. 0065.
76. E. Kleban, C. M. W. Tax, U. S. Rudrapatna, D. K. Jones and R. Bowtell, *Neuroimage*, 2020, **217**, 116793. PubMed PMID: 32335263.
77. Y. Nam, J. Lee, D. Hwang and D.-H. Kim, *Neuroimage*, 2015, **116**, 214–221. PubMed PMID: 25858448.
78. E. Alonso-Ortiz, I. R. Levesque and G. B. Pike, *Neuroimage*, 2018, **182**, 370–378. PubMed PMID: 28958882.
79. P. T. Callaghan, *Principles of nuclear magnetic resonance microscopy*, Oxford University Press on demand, 1993.
80. H. Celik, M. Bouhrara, D. A. Reiter, K. W. Fishbein and R. G. Spencer, *Stabilization of the inverse Laplace transform of multiexponential decay through introduction of a second dimension*, 2013, vol. 236.
81. I. O. Jelescu, J. Veraart, E. Fieremans and D. S. Novikov, *NMR Biomed.*, 2016, **29**, 33–47. PubMed PMID: 26615981.
82. T. Niendorf, R. M. Dijkhuizen, D. G. Norris, M. van Lookeren Campagne and K. Nicolay, *Magn. Reson. Med.*, 1996, **36**, 847–857. PubMed PMID: 8946350.
83. E. McKinnon and J. Jensen, in *ISMRM*, 2019, p. 1117.
84. E. O. Stejskal and J. E. Tanner, *J. Chem. Phys.*, 1965, **42**, 288–292.
85. J. P. de Almeida Martins and D. Topgaard, *Sci. Rep.*, 2018, **8**, 2488. PubMed PMID: 29410433.
86. J. L. Boxerman, L. M. Hamberg, B. R. Rosen and R. M. Weisskoff, *Magn. Reson. Med.*, 1995, **34**, 555–566. PubMed PMID: 8524024.
87. L. A. Stables, R. P. Kennan and J. C. Gore, *Magn. Reson. Med.*, 1998, **40**, 432–442. PubMed PMID: 9727947.
88. D. van Dusschoten, P. A. de Jager and H. van As, *J. Magn. Reson. Ser. A*, 1995, **112**, 237–240.
89. W. David Williams, E. F. . Seymour and R. . Cotts, *J. Magn. Reson.*, 1978, **31**, 271–282.
90. J. E. Tanner, *J. Chem. Phys.*, 1970, **52**, 2523–2526.

91. L. J. C. Peschier, J. A. Bouwstra, J. de Bleyser, H. E. Junginger and J. C. Leyte, *Biomaterials*, 1993, **14**, 945–952. PubMed PMID: 8268387.
92. A. A. Istratov and O. F. Vyvenko, *Rev. Sci. Instrum.*, 1999, **70**, 1233–1257.
93. M. Bertero, P. Boccacci and E. R. Pike, *Proc. R. Soc. London A Math. Phys. Eng. Sci.*
94. G. H. Weiss, R. K. Guptaj, J. A. Ferretti and E. D. Becker, *J. Magn. Reson.*, 1980, **37**, 369–379.
95. J. A. Jones, P. Hodgkinson, A. L. Barker and P. J. Hore, *J. Magn. Reson. Ser. B*, 1996, **113**, 25–34.
96. M. D. Does and J. C. Gore, *NMR Biomed.*, 2000, **13**, 1–7. PubMed PMID: 10668048.
97. D. K. Jones, *Magn. Reson. Med.*, 2004, **51**, 807–815. PubMed PMID: 15065255.
98. E. Caruyer, C. Lenglet, G. Sapiro and R. Deriche, *Magn. Reson. Med.*, 2013, **69**, 1534–1540. PubMed PMID: 23625329.
99. S. Coelho, J. M. Pozo, S. N. Jespersen and A. F. Frangi, .
100. M. Afzali, C. M. W. Tax, C. Chatziantoniou and D. K. Jones, in *ISBI*, 2019, p. WeS54.2.
101. S. Ahola, V. V Zhivonitko, O. Mankinen, G. Zhang, A. M. Kantola, H.-Y. Chen, C. Hilty, I. V. Koptyug and V.-V. Telkki, *Nat. Commun.*, 2015, **6**, 8363. PubMed PMID: 26381101.
102. D. K. Jones, D. C. Alexander, R. Bowtell, M. Cercignani, F. Dell'Acqua, D. J. McHugh, K. L. Miller, M. Palombo, G. J. M. Parker, U. S. Rudrapatna and C. M. W. Tax, *Neuroimage*, , DOI:10.1016/J.NEUROIMAGE.2018.05.047.
103. K. Setsompop, R. Kimmlingen, E. Eberlein, T. Witzel, J. Cohen-Adad, J. A. McNab, B. Keil, M. D. Tisdall, P. Hoecht, P. Dietz, S. F. Cauley, V. Tountcheva, V. Matschl, V. H. Lenz, K. Heberlein, A. Potthast, H. Thein, J. Van Horn, A. Toga, F. Schmitt, D. Lehne, B. R. Rosen, V. Wedeen and L. L. Wald, *Neuroimage*, 2013, **80**, 220–233. PubMed PMID: 23707579.
104. Q. Fan, S. Y. Huang, A. Nummenmaa, T. Witzel and L. L. Wald, in *ISMRM*, 2017, p. 1757.
105. L. Mueller, S. U. Rudrapatna, C. M. W. Tax, R. Wise and D. K. Jones, in *ISMRM*, 2019, p. 0766.
106. C. M. W. Tax, U. S. Rudrapatna, L. Mueller and D. K. Jones, in *ISMRM*, 2019, p. 1115.
107. J. H. Lee, C. Labadie, C. S. Springer and G. S. Harbison, *J. Am. Chem. Soc.*, 1993, **115**, 7761–7764.
108. Y.-Q. Song, L. Venkataramanan, M. D. Hürlimann, M. Flaum, P. Frulla and C. Straley, *J. Magn. Reson.*, 2002, **154**, 261–268. PubMed PMID: 11846583.
109. D. Topgaard, *J. Magn. Reson.*, 2017, **275**, 98–113. PubMed PMID: 28040623.
110. B. Jian, B. C. Vemuri, E. Özarslan, P. R. Carney and T. H. Mareci, *Neuroimage*, 2007, **37**, 164–176. PubMed PMID: 17570683.
111. A. D. Leow, S. Zhu, L. Zhan, K. McMahon, G. I. de Zubicaray, M. Meredith, M. J. Wright, A. W. Toga and P. M. Thompson, *Magn. Reson. Med.*, 2009, **61**, 205–214. PubMed PMID: 19097208.
112. C.-F. Westin, H. Knutsson, O. Pasternak, F. Szczepankiewicz, E. Özarslan, D. van Westen, C. Mattisson, M. Bogren, L. J. O'Donnell, M. Kubicki, D. Topgaard and M. Nilsson, *Neuroimage*, 2016, **135**, 345–62. PubMed PMID: 26923372.
113. B. Scherrer, A. Schwartzman, M. Taquet, M. Sahin, S. P. Prabhu and S. K. Warfield, *Magn. Reson. Med.*, 2016, **76**, 963–977. PubMed PMID: 26362832.
114. I. Fredholm, *Acta Math.*, 1903, **27**, 365–390.
115. K. P. Whittall and A. L. MacKay, *J. Magn. Reson.*, 1989, **84**, 134–152.
116. R. M. Kroeker and R. Mark Henkelman, *J. Magn. Reson.*, 1986, **69**, 218–235.
117. N. Ostrowsky, D. Sornette, P. Parker and E. R. Pike, *Opt. Acta Int. J. Opt.*, 1981, **28**, 1059–1070.
118. A. Cloninger, W. Czaja, R. Bai and P. J. Basser, *SIAM J. Imaging Sci.*, 2014, **7**, 1775–1798.
119. R. Bai, A. Cloninger, W. Czaja and P. J. Basser, *J. Magn. Reson.*, 2015, **255**, 88–99. PubMed PMID: 25917134.
120. J. Mitchell and E. J. Fordham, *J. Magn. Reson.*, 2011, **212**, 394–401. PubMed PMID: 21875819.
121. M. Yang, D. Ma, Y. Jiang, J. Hamilton, N. Seiberlich, M. A. Griswold and D. McGivney, *Magn. Reson. Med.*, 2018, **79**, 2392–2400. PubMed PMID: 28804918.
122. C. L. Lawson and R. J. Hanson, *Solving Least Squares Problems*, Society for Industrial and Applied Mathematics, 1995.
123. S. W. Provencher, *Comput. Phys. Commun.*, 1982, **27**, 213–227.

124. A. Daducci, E. J. Canales-Rodríguez, H. Zhang, T. B. Dyrby, D. C. Alexander and J.-P. Thiran, *Neuroimage*, 2015, **105**, 32–44. PubMed PMID: 25462697.
125. M. Urbańczyk, D. Bernin, W. Koźmiński and K. Kazimierczuk, *Anal. Chem.*, 2013, **85**, 1828–1833. PubMed PMID: 23297715.
126. D. Benjamini and P. J. Basser, *Microporous Mesoporous Mater.*, 2018, **269**, 93–96. PubMed PMID: 30220874.
127. Má. A. T. Figueiredo, R. D. Nowak and S. J. Wright, *IEEE J. Sel. Top. Signal Process.*, 2007, **1**, 586–597.
128. J. Mitchell, T. C. Chandrasekera and L. F. Gladden, *Prog. Nucl. Magn. Reson. Spectrosc.*, 2012, **62**, 34–50. PubMed PMID: 22364615.
129. G. H. Golub, M. Heath and G. Wahba, *Technometrics*, 1979, **21**, 215.
130. P. Hansen, *IMM, Dep. Math. Model. Tech. Univ. Denmark*.
131. B. Sun and K.-J. Dunn, *J. Magn. Reson.*, 2005, **172**, 152–160. PubMed PMID: 15589418.
132. J. Mitchell, J. Staniland, R. Chassagne and E. J. Fordham, *Transp. Porous Media*, 2012, **94**, 683–706.
133. US6960913B2, 2005.
134. D. S. Novikov, V. G. Kiselev and S. N. Jespersen, *Magn. Reson. Med.*, 2018, **79**, 3172–3193. PubMed PMID: 29493816.
135. R. J. S. Brown, G. C. Borgia, P. Fantazzini and E. Mesini, *Magn. Reson. Imaging*, 1991, **9**, 687–693.
136. E. Panagiotaki, T. Schneider, B. Siow, M. G. Hall, M. F. Lythgoe and D. C. Alexander, *Neuroimage*, 2012, **59**, 2241–2254. PubMed PMID: 22001791.
137. D. S. Tuch, T. G. Reese, M. R. Wiegell, N. Makris, J. W. Belliveau and V. J. Wedeen, *Magn. Reson. Med.*, 2002, **48**, 577–582. PubMed PMID: 12353272.
138. T. E. J. Behrens, M. W. Woolrich, M. Jenkinson, H. Johansen-Berg, R. G. Nunes, S. Clare, P. M. Matthews, J. M. Brady and S. M. Smith, *Magn. Reson. Med.*, 2003, **50**, 1077–1088. PubMed PMID: 14587019.
139. H. Zhang, T. Schneider, C. A. Wheeler-Kingshott and D. C. Alexander, *Neuroimage*, 2012, **61**, 1000–1016. PubMed PMID: 22484410.
140. A. Szafer, J. Zhong and J. C. Gore, *Magn. Reson. Med.*, 1995, **33**, 697–712. PubMed PMID: 7596275.
141. S. Lasič, F. Szczepankiewicz, S. Eriksson, M. Nilsson and D. Topgaard, *Front. Phys.*, 2014, **2**, 11.
142. M. Röding, D. Bernin, J. Jonasson, A. Särkkä, D. Topgaard, M. Rudemo and M. Nydén, *J. Magn. Reson.*, 2012, **222**, 105–111. PubMed PMID: 22864268.
143. J. H. Jensen and J. A. Helpern, *NMR Biomed.*, 2010, **23**, 698–710. PubMed PMID: 20632416.
144. B. D. Boss, E. O. Stejskal and J. D. Ferry, *J. Phys. Chem.*, 1967, **71**, 1501–1506.
145. K. J. Packer and C. Rees, *J. Colloid Interface Sci.*, 1972, **40**, 206–218.
146. P. J. Basser, J. Mattiello and D. Lebihan, *J. Magn. Reson. Ser. B*, 1994, 103, 247–254. PubMed PMID: 8019776.
147. F. Szczepankiewicz, D. van Westen, E. Englund, C.-F. Westin, F. Ståhlberg, J. Lätt, P. C. Sundgren and M. Nilsson, *Neuroimage*, 2016, **142**, 522–532. PubMed PMID: 27450666.
148. A. Reymbaut, B. Scherrer, G. Gilbert, F. Szczepankiewicz, M. Nilsson and M. Descoteaux, in *ISMRM*, 2018, p. 0257.
149. D. S. Novikov, E. Fieremans, S. N. Jespersen and V. G. Kiselev, *NMR Biomed.*, 2018, e3998.
150. J.-D. Tournier, F. Calamante and A. Connelly, *Neuroimage*, 2007, **35**, 1459–1472. PubMed PMID: 17379540.
151. C. M. W. Tax, B. Jeurissen, S. B. Vos, M. A. Viergever and A. Leemans, *Neuroimage*, , DOI:10.1016/j.neuroimage.2013.07.067.
152. D. E. Koppel, *J. Chem. Phys.*, 1972, **57**, 4814–4820.
153. V. G. Kiselev, in *Diffusion MRI*, Oxford University Press, 2010, pp. 152–168.
154. B. Håkansson, M. Nydén and O. Söderman, *Colloid Polym. Sci.*, 2000, **278**, 399–405.
155. J. H. Jensen, J. A. Helpern, A. Ramani, H. Lu and K. Kaczynski, *Magn. Reson. Med.*, 2005, **53**, 1432–1440. PubMed PMID: 15906300.
156. A. Chuhutin, B. Hansen and S. N. Jespersen, *NMR Biomed.*, , DOI:10.1002/nbm.3777.
157. L. Venkataramanan, F. K. Gruber, T. M. Habashy and D. E. Freed, *J. Magn. Reson.*, 2010, **206**, 20–31. PubMed PMID: 20576455.

158. M. Prange and Y.-Q. Song, *J. Magn. Reson.*, 2009, **196**, 54–60. PubMed PMID: 18952474.
159. S. Geman and D. Geman, *IEEE Trans. Pattern Anal. Mach. Intell.*, 1984, **PAMI-6**, 721–741.
160. D. C. Alexander, *Magn. Reson. Med.*, 2008, **60**, 439–448. PubMed PMID: 18666109.
161. D. C. Alexander, P. L. Hubbard, M. G. Hall, E. A. Moore, M. Ptito, G. J. M. Parker and T. B. Dyrby, *Neuroimage*, 2010, **52**, 1374–1389. PubMed PMID: 20580932.
162. S. N. Sotiropoulos, S. Jbabdi, J. L. Andersson, M. W. Woolrich, K. Ugurbil and T. E. J. Behrens, *IEEE Trans. Med. Imaging*, 2013, **32**, 969–982. PubMed PMID: 23362247.
163. R. L. Harms and A. Roebroeck, *Front. Neuroinform.*, 2018, **12**, 97. PubMed PMID: 30618702.
164. B. Jeurissen, A. Leemans, D. K. Jones, J.-D. Tournier and J. Sijbers, *Hum. Brain Mapp.*, 2011, **32**, 461–479. PubMed PMID: 21319270.
165. D. K. Jones and C. Pierpaoli, *Magn. Reson. Med.*, 2005, **53**, 1143–1149. PubMed PMID: 15844149.
166. C. M. W. Tax, C.-F. Westin, T. Dela Haije, A. Fuster, M. A. Viergever, E. Calabrese, L. Florack and A. Leemans, *Med. Image Anal.*, , DOI:10.1016/j.media.2017.03.007.
167. P. T. Callaghan, D. MacGowan, K. J. Packer and F. O. Zelaya, *J. Magn. Reson.*, 1990, **90**, 177–182.
168. V. J. Wedeen, R. P. Wang, J. D. Schmahmann, T. Benner, W. Y. I. Tseng, G. Dai, D. N. Pandya, P. Hagmann, H. D'Arceuil and A. J. de Crespigny, *Neuroimage*, 2008, **41**, 1267–1277. PubMed PMID: 18495497.
169. M. M. Britton, R. G. Graham and K. J. Packer, *J. Magn. Reson.*, 2004, **169**, 203–214. PubMed PMID: 15261615.
170. K. E. Washburn and P. T. Callaghan, *J. Magn. Reson.*, 2007, **186**, 337–340. PubMed PMID: 17376720.
171. E. Fieremans and H.-H. Lee, *Neuroimage*, 2018, **182**, 39–61. PubMed PMID: 29920376.
172. I. O. Jelescu and M. D. Budde, *Front. Phys.*, 2017, **5**, 61.
173. X. Ranhong and X. Lizhi, *Pet.Sci*, 2011, **8**, 163–169.
174. K. R. Brownstein and C. E. Tarr, *Phys. Rev. A*, 1979, **19**, 2446–2453.
175. P. T. Callaghan, *J. Magn. Reson. Ser. A*, 1995, **113**, 53–59.
176. P. T. Callaghan, *J. Magn. Reson.*, 1997, **129**, 74–84. PubMed PMID: 9405218.
177. S. L. Codd and P. T. Callaghan, *J. Magn. Reson.*, 1999, **137**, 358–372. PubMed PMID: 10089170.
178. I. Drobnjak, H. Zhang, M. G. Hall and D. C. Alexander, *J. Magn. Reson.*, 2011, **210**, 151–157. PubMed PMID: 21435926.
179. A. Caprihan, L. Z. Wang and E. Fukushima, *J. Magn. Reson. Ser. A*, 1996, **118**, 94–102.
180. P. T. Callaghan, S. Godefroy and B. N. Ryland, *J. Magn. Reson.*, 2003, **162**, 320–327. PubMed PMID: 12810015.
181. L. Marinelli, M. D. Hürlimann and P. N. Sen, *J. Chem. Phys.*, 2003, **118**, 8927–8940.
182. E. G. Novikov, D. van Dusschoten and H. Van As, *J. Magn. Reson.*, 1998, **135**, 522–528. PubMed PMID: 9878479.
183. L. van der Weerd, S. M. Melnikov, F. J. Vergeldt, E. G. Novikov and H. Van As, *J. Magn. Reson.*, 2002, **156**, 213–221. PubMed PMID: 12165256.
184. E. Fieremans, A. Pires and J. H. Jensen, *Magn. Reson. Med.*, 2012, **68**, 537–542. PubMed PMID: 22161496.
185. M. Nilsson, J. Larsson, D. Lundberg, F. Szczepankiewicz, T. Witzel, C.-F. Westin, K. Bryskhe and D. Topgaard, *Magn. Reson. Med.*, 2018, **79**, 1817–1828. PubMed PMID: 28686785.
186. C. M. W. Tax, F. Szczepankiewicz, M. Nilsson and D. K. Jones, *bioRxiv*, 2019, 584730.
187. C. S. Johnson, *J. Magn. Reson. Ser. A*, 1993, **102**, 214–218.
188. P. T. Callaghan and I. Furó, *J. Chem. Phys.*, 2004, **120**, 4032–4038. PubMed PMID: 15268569.
189. K. E. Washburn and P. T. Callaghan, *Phys. Rev. Lett.*, , DOI:10.1103/PhysRevLett.97.175502.
190. S. St-Jean, P. Coupé and M. Descoteaux, *Med. Image Anal.*, 2016, **32**, 115–30. PubMed PMID: 27082655.
191. J. Veraart, D. S. Novikov, D. Christiaens, B. Ades-aron, J. Sijbers and E. Fieremans, *Neuroimage*, 2016, **142**, 394–406. PubMed PMID: 27523449.
192. S. Aja-Fernández and G. Vegas-Sánchez-Ferrero, *Statistical Analysis of Noise in MRI*, Springer International Publishing, Cham, 2016.
193. Y.-Q. Song, L. Zielinski and S. Ryu, *Phys. Rev. Lett.*, 2008, **100**, 248002. PubMed PMID: 18643630.
194. D. Bernin and D. Topgaard, *Curr. Opin. Colloid Interface Sci.*, 2013, **18**, 166–172.

195. M. J. Knight, B. Wood, E. Couthard and R. Kauppinen, *Biomed. Spectrosc. Imaging*, 2015, **4**, 299–310.
196. P. J. Slator, J. Hutter, R. V. Marinescu, M. Palombo, A. L. Young, L. H. Jackson, A. Ho, L. C. Chappell, M. Rutherford, J. V. Hajnal and D. C. Alexander, in *IPMI*, Springer, Cham, 2019, pp. 755–766.

License